WL-TR-93-4107

**AD-A274 235**

AN X-RAY ABSORPTION FINE STRUCTURE
STUDY OF ORDERING IN POLYTHIOPHENE
THIN FILMS

Guy A. DeRose
H. Jiang
P. D. Haaland
Lawrence Associates, Inc.
5100 Springfield Pike
Dayton, OH 45431

W. W. Adams
T. J. Bunning
Hardened Materials Branch

R. W. Hoffman
C. A. Zorman
Dept. of Physics
Case Western Reserve University
Cleveland, OH 44106-7079

**S DTIC**
**ELECTE**
**DEC 2 8 1993**
**A**

September 1993

Interim Report for the Period January 1993 - September 1993

Approved for public release;  distribution unlimited

Materials Directorate
Wright Laboratory
Air Force Materiel Command
Wright-Patterson Air Force Base, Ohio 45433-7702
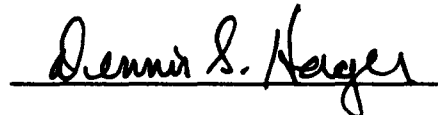
**93 12 23 004**

**93-31147**

## NOTICE

When Government drawings, specifications, or other data are used for any purpose other than in connection with a definitely Government-related procurement, the United States Government incurs no responsibility or any obligation whatsoever. The fact that the Government may have formulated or in any way supplied the said drawings, specifications, or other data, is not to be regarded by implication, or otherwise in any manner construed, as licensing the holder, or any other person or corporation; or as conveying any rights or permission to manufacture, use, or sell any patented invention that may in any way be related thereto.

This report is releasable to the National Technical Information Service (NTIS). At NTIS, it will be available to the general public, including foreign nations.

This technical report has been reviewed and is approved for publication.

WADE ADAMS, Engineer
Optical Materials Survivability
Hardened Materials Branch

DENNIS S. HAGER, Acting Chief
Hardened Materials Branch
Electromagnetic Materials and
Survivability Division

WILLIAM R. WOODY, Chief
Electromagnetic Materials and
Survivability Division

If your address has changed, if you wish to be removed from our mailing list, or if the addressee is no longer employed by your organization please notify WL/MLPJ, Wright-Patterson AFB, OH 45433-7702 to help maintain a current mailing list.

Copies of this report should not be returned unless return is required by security considerations, contractual obligations, or notice on a specific document.

# REPORT DOCUMENTATION PAGE

| 1. AGENCY USE ONLY *(Leave Blank)* | 2. REPORT DATE September 1993 | 3. REPORT TYPE AND DATES COVERED INTERIM 01/01/93--09/01/93 |
|---|---|---|

**4. TITLE AND SUBTITLE**

AN X-RAY ABSORPTION FINE STRUCTURE STUDY OF ORDERING IN POLYTHIOPHENE THIN FILMS

**5. FUNDING NUMBERS**

PE 62102
PR 2422
TA 04
WU 01

**6. AUTHOR(S)**

G.A. DeROSE, H. JIANG, C.A. ZORMAN
W.W. ADAMS, T.J. BUNNING,
R.W. HOFFMAN P. D. HAALAND

**7. PERFORMING ORGANIZATION NAME(S) AND ADDRESS(ES)**

LAWRENCE ASSOCIATES, INCORPORATED
5100 SPRINGFIELD PIKE, SUITE509
DAYTON, OH 45401

**8. PERFORMING ORGANIZATION REPORT NUMBER**

**9. SPONSORING MONITORING AGENCY NAME(S) AND ADDRESS(ES)**

MATERIALS DIRECTORATE
WRIGHT LABORATORY
AIR FORCE MATERIEL COMMAND
WRIGHT PATTERSON AFB OH 45433-7734

**10. SPONSORING/MONITORING AGENCY REP NUMBER**

WL-TR-93-4107

**11. SUPPLEMENTARY NOTES**

**12a. DISTRIBUTION/AVAILABILITY STATEMENT**

APPROVED FOR PUBLIC RELEASE; DISTRIBUTION IS UNLIMITED.

**12b. DISTRIBUTION CODE**

**13. ABSTRACT**

Thin film organic nonlinear optical (NLO) materials are being investigated for laser hardening applications due to their enhanced processability. Plasma-polymerized thiophene films formed by the flowing afterglow synthesis of polyaromatic heterocycles allow one to modulate the refractive index profile in real-time, thus allowing an organ.. analog of a rugate to be realized. Since the relationships between the molecular structure, NLO response, and proces..g conditions are poorly understood, the feasibility of using X-ray Absorption Fine Structure (XAFS) spectroscop.. examined. This method allows the local environment of X-ray absorbing atoms in polythiophene and plasma-polymerized 2,5 dichlorothiophene and 2,5 dibromothiophene thin films at the sulfur (S) K-edge and, as appropriate, the chlorine (Cl) and bromine (Br) K-edges to be probed. Argon absorption was found to limit the data range of the S and Cl edge data. The Br K-edge data indicated that the local Br environment was maintained in the plasma-polymerized films of 2,5 dibromothiophene within experimental error. As a result, XAFS spectroscopy has been shown to be a useful technique for investigating the molecular structure of an important category of nonlinear optical materials.

**14. SUBJECT TERMS**

XAFS, Thiophene, Synchrotron Radiation, X-Ray Absorption, Nonlinear Optics, Thin Films

**15. NUMBER OF PAGES**

**16. PRICE CODE**

| 17. SECURITY CLASSIFICATION OF REPORT UNCLASSIFIED | 18. SECURITY CLASS OF THIS PAGE. UNCLASSIFIED | 19. SECURITY CLASS OF ABSTRACT UNCLASSIFIED | 20. LIMITATION ABSTRACT UL |
|---|---|---|---|

# FOREWORD

DTIC QUALITY INSPECTED 8

| Accesion For | | |
|---|---|---|
| NTIS CRA&I | | ☑ |
| DTIC TAB | | ☐ |
| Unannounced | | ☐ |
| Justification | | |
| By | | |
| Distribution / | | |
| Availability Codes | | |
| Dist | Avail and / or Special | |
| A-1 | | |

iii

# TABLE OF CONTENTS

# LIST OF ILLUSTRATIONS

# LIST OF TABLES

# Section 1

# INTRODUCTION

Nonlinear optical (NLO) materials offer great promise in the search for a solution to the problem of laser hardening, which is the ability of a material to stop a laser beam. The intense optical fields produced by a laser are capable of inducing both second- ($\chi^{(2)}$) and third-order ($\chi^{(3)}$) NLO effects including phase conjugation or modulation, frequency doubling or tripling, and optical limiting and switching [1-3]. These last two phenomena are currently being investigated as they have possible laser hardening applications in both thin film and solution-based limiting systems.

Organic compounds have received considerable attention as NLO materials due to the potential capability to synthetically design and tailor the molecular electronic environment to optimize *molecular-level* NLO responses. However, the ability to control the local environment around the NLO chromophore is key in optimizing the *bulk* NLO signal while maximizing transparency by minimizing optical scatter. Although solvent-based optical limiting systems are self-healing over long time scales, incorporation of nonlinear materials into thin films is preferred due to engineerable thermal and mechanical properties. Since the molecular quantities ultimately depend on the microstructure at the near-atomic level, the structure on both the molecular and macromolecular scales becomes important in defining the usable limitations of a material. In the case of an amorphous polymer this becomes especially challenging, and a methodology must be developed by which to infer the microstructure to allow optimization of an optical response by design.

This study addresses structure determination at the molecular level in amorphous polymers using X-ray absorption techniques. Various systems are currently being evaluated by the Laser Hardened Materials Branch of the Wright Laboratory for the generation of novel devices and materials for laser hardened optical systems in response to USAF requirements for laser protection.

1

One such system is polythiophene (PT) and substituted PT films formed by the flowing afterglow synthesis of polyaromatic heterocycles. This novel synthetic technique produces films that are much denser and smoother than those produced from conventionally synthesized polythiophene[4]. This allows for high NLO responses to be observed. These films have been characterized by Rutherford backscattering spectroscopy (RBS), optical absorption, scanning force microscopy, and spectroscopic ellipsometry [4]. The thiophene monomer can assume different conformations along a given chain. Since the conformation of these rings and the relationship of neighboring chains ultimately affect the nonlinear optical properties of the bulk film, it is desirable to be able to examine the local environment of the neighboring sulfur atoms. Specifically, are the rings in a single chain randomly ordered or do they have cis or trans local order?
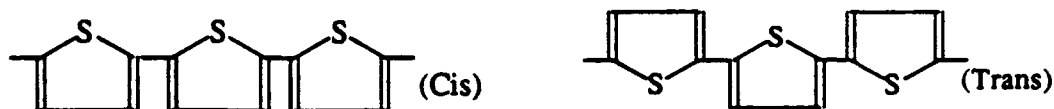


This consideration is important in increasing the molecular susceptibility of this conjugated, highly delocalized system [5]. This can be extrapolated to include investigating how the sulfur atoms in one chain pack with respect to their nearest neighbors in another chain. The deposition process is illustrated in Figure 1, which shows how the Cl end-caps are released into the gas phase upon polymerization of the film. A similar process takes place for the Br-substituted materials.
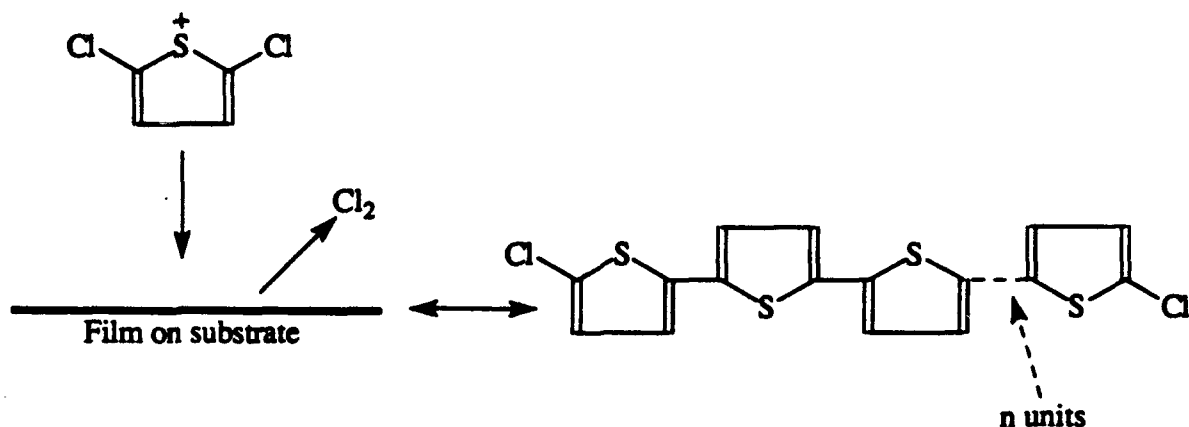
Figure 1: Schematic diagram of the Plasma - Enhanced Chemical Vapor Deposition (PECVD) process. The large chain to the right is only representative of a chain in the deposited film and is intended to illustrate the Cl end - caps and that most of the Cl from the monomers is given off as $Cl_2$. Adapted from reference [4].

To examine the local structure, order, and coordination of S in polythiophene, and Br and Cl in the substituted polythiophene systems, we used X-ray absorption fine structure (XAFS) as a characterization tool [6] since it is sensitive to short range order ($\leq 10\text{Å}$ from the absorbing atom) and to the absorbing species. Data from the extended XAFS (EXAFS) region ($E \geq E_O + 50$ eV) was analyzed to investigate the local environment seen by the S, Cl and Br atoms, and will be presented in Section 5. Additional information, such as chain length, can be inferred by analysis of edge jumps and will also be discussed. The neighboring species, coordination number, radial distribution, and relative disorder for multiple shells will be examined.

3

## Section 2

## THEORY AND BACKGROUND

### 2.1  X-Ray Absorption Fine Structure

When a photon interacts with matter, three distinct processes may be observed: 1) photoelectron emission, 2) Compton scattering, and 3) electron-positron pair production. The extent to which each of these processes occurs depends both on the photon energy and the properties of the material with which the photon interacts [7], as shown in Figure 2.
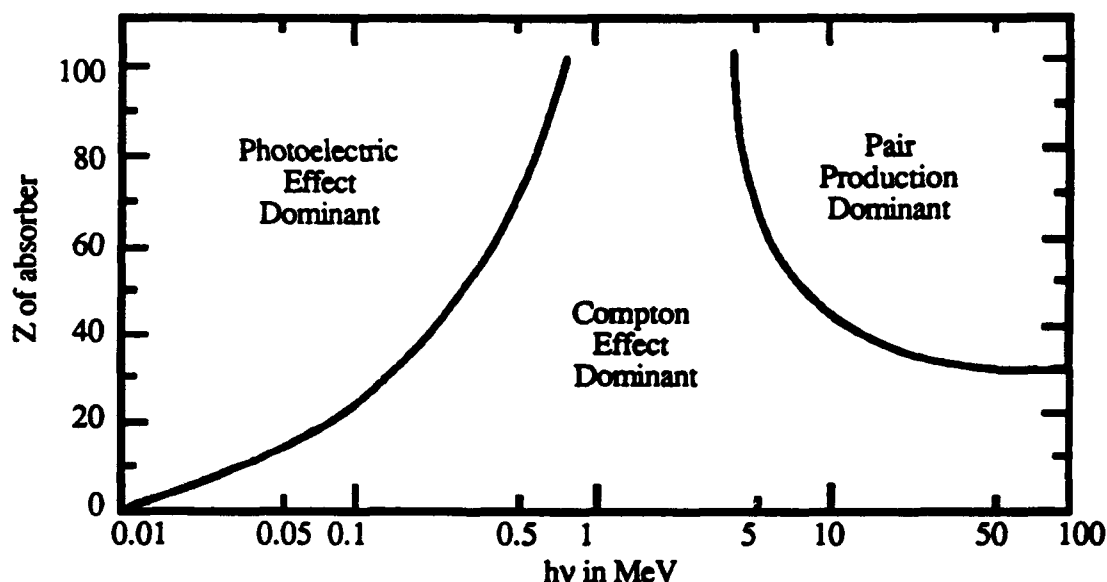


Figure 2:    The relative importance of the three major types of photon interactions in matter. The lines show the values of atomic number Z and photon energy hv for which the neighboring effects are equal. Adapted from Feldman and Mayer (ref. 7).

The extended X-ray absorption fine structure (EXAFS) arises from oscillations in the photoelectric cross-section or absorption coefficient as a function of photoelectron energy or wave number due to scattering of the ejected photoelectron by atoms surrounding the absorbing atom [8]. EXAFS only occurs when atoms are in a condensed state, since a photoelectron arising from

absorption by an isolated atom has no neighboring atoms from which to backscatter and produce interference.

A detailed review and physical description of X-ray absorption are given by Stern [9], and some of the highlights of that theory are presented here. X-ray absorption is dominated by the photoelectric effect in the energy region most often thought of as X-rays (up to approximately 40 keV) and is the process by which a photon has enough energy to free an electron from a bound state in the atom. The energy which just allows this transition to take place is called the absorption edge. A typical absorption edge is shown in Figure 3, with various features of interest marked on the plot. These will become useful in Section 5.3.1.1 in the discussion on edge jump analysis.
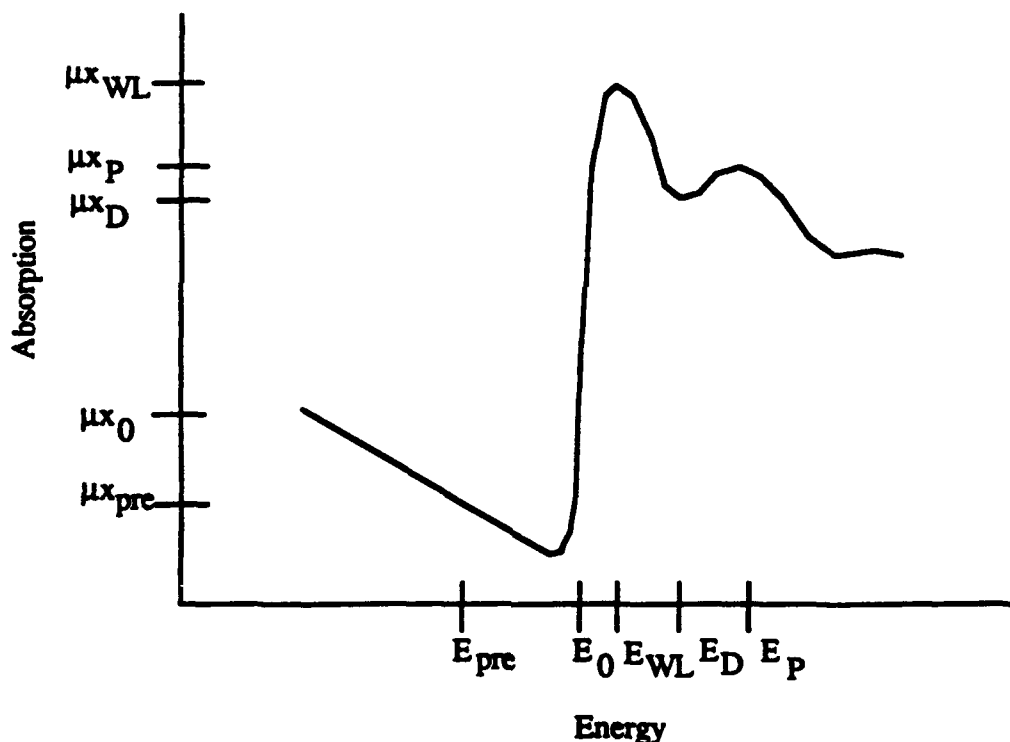


Figure 3: Typical absorption edge shape. Pre, 0, WL, D and P refer to the pre-edge, edge, white line, "dip," and "peak" energies or absorptions, respectively, as shown in the figure.

Quantum mechanically, if the electron originates in the $n=1$ shell the absorption edge is the K-edge and for $n=2$ the L-edges. There are 3 L-edges since for $n=2$ there are 3 initial states: $2s$ ($L_I$), $2p_{3/2}$ ($L_{III}$), and $2p_{1/2}$ ($L_{II}$). If we assume that all of the photon's energy is used to excite a

6

single core electron, then that electron's kinetic energy is just the difference between the incident photon's energy hv and the electron's binding energy $E_0$. For a photoelectron whose kinetic energy is large (approximately 15 eV) compared with its interaction with the surrounding atoms (approximately 3 eV), the interaction of the photoelectron with its surroundings may be treated as a perturbation about an isolated atom. To first order, the final state is modified by a single scattering from each surrounding atom.

In a more formal sense, the absorption is given as the matrix element between the initial and final states of the atom, where the initial state is the electron in the core and the final state is the outgoing photoelectron. Since the core state wave function is nonzero only in the core, then the matrix element is nonzero only there as well. So, one only needs to determine how the surrounding atoms modify the photoelectron's wave function near the center of the absorbing (central) atom to obtain the EXAFS function. As shown in Figure 4, the backscattered waves will interfere with the emitted photoelectron wave and the energy dependence of this interference contains the structural information, since the relative phase of the two waves results in the interference.
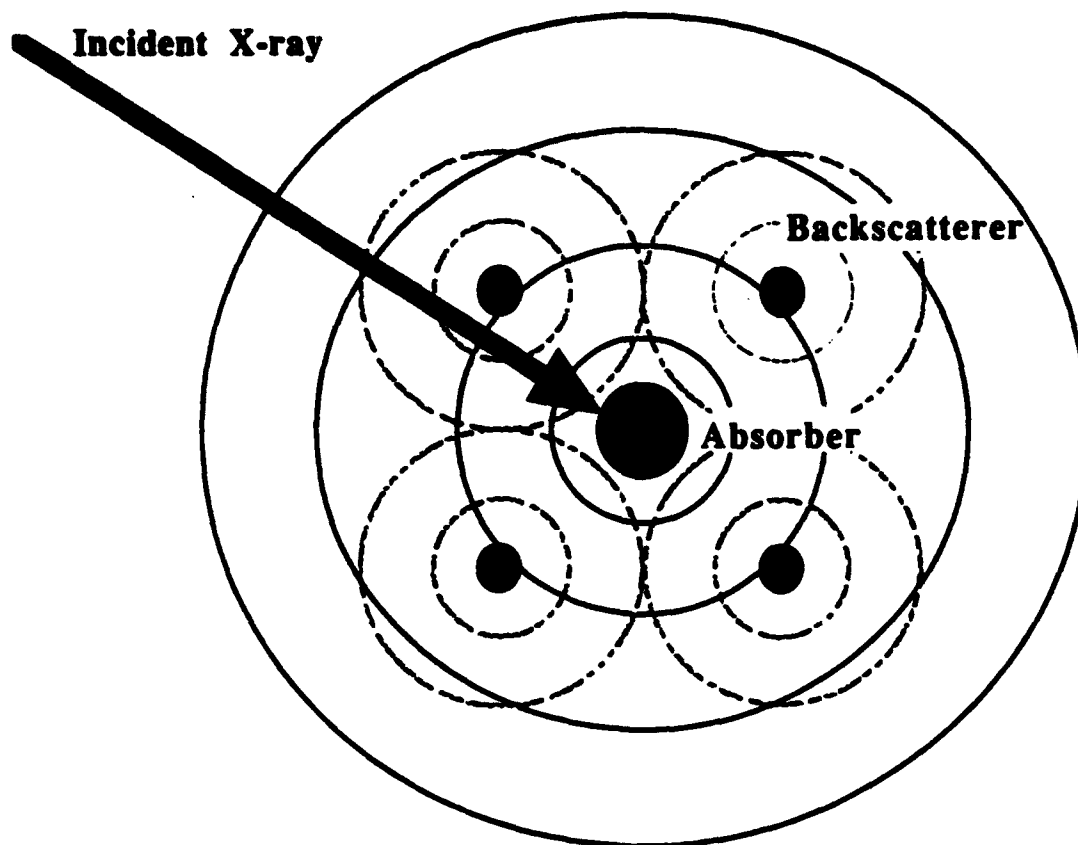
**Figure 4:** Interference between outgoing and backscattered photoelectrons generated by incident X-ray being absorbed by central atom setting up photoelectron emission.

This phase depends on the distance between the absorbing and backscattering atoms and the type of atoms surrounding the absorber. The EXAFS oscillations are explained in terms of phase: peaks in the fine structure oscillations correspond to photo- and backscattered electrons being in phase and troughs to photo- and backscattered electrons being out of phase.

It has been determined [8,10] that for energies sufficiently high above the absorption edge ($\geq$ 50 eV) the single scattering approximation adequately describes the structure and that the photoelectron wave functions can be treated by the plane wave approximation. The EXAFS oscillations, following the single-scattering and outgoing plane wave approaches, are given for K-edges as a function of photoelectron wave number k by [9]

$$\chi(k) = \sum_i \frac{N_i}{kR_i^2} S_0^2 A(k) F_i(\pi, k, R) e^{-2((R_i - \Delta)/\lambda)} e^{-2\sigma_i^2 k^2} \sin[2kR_i + 2\delta(k) + \phi_i(k)] \quad (1)$$

8

where $N_i$ is the number of equivalent scatterers of type $i$ a mean distance $R_i$ from the absorber, $F_i(\pi,k,R)$ is the (energy dependent) backscattering function, $e^{-2k^2\sigma_i^2}$ is a Debye-Waller term describing both static (structural) and thermal disorder, $e^{-2((R_i-\Delta)/\lambda)}$ is a term which accounts for inelastic scattering effects over the photoelectron mean free path $\lambda$ modified by the "core radius" $\Delta$, $S_0^2$ is an amplitude reduction factor representing relaxation of the central atom wave function due to "passive" electrons not participating in the absorption process [11], and $\sin[2kR_i+2\delta(k)+\phi_i(k)]$ is the interference term, where $\phi_i(k)$ is the (energy dependent) phase shift. The reader should note that $\sigma^2$ is not the same as the Debye-Waller term in X-ray diffraction (XRD) which is a mean square deviation about the lattice site for each atom, while in EXAFS this deviation is a relative one between the absorbing and backscattering atoms [9]. The photoelectron wave number, k, is given by $k = \frac{2\pi}{h}\sqrt{2m(E-E_0)}$, where m is the mass of the electron, E is the incident X-ray energy, and $E_0$ is the edge energy.

Fourier transformation into R-space provides a measure of the radial distribution function for the neighborhood of the absorbing species. The Fourier Transform of $\chi(k)$ is $\phi(r)$ and is given by

$$\phi_n(r) = \frac{1}{\sqrt{2\pi}}\int_{k_{min}}^{k_{max}} k^n\chi(k)e^{2ikr}dk \qquad (2)$$

where n is the index for $k^n$ weighting of the transform and $k_{min}$ and $k_{max}$ are the lower and upper bounds of the usable data, respectively, in k space. In practice n is chosen to be either 1 or 3. For n=1, the transform is very sensitive to the choice of $k_{min}$, especially for small r. This transform is related to spatial variation of a scattering matrix [12]. In the case of n=3, which is related to a pseudo-charge density, the transform is reasonably insensitive to the choice of $k_{min}$ and inner potential, since it places less weight on the low energy portion of $\chi(k)$ which is where more uncertainties occur. Even though the $k^3$ - weighted data are in better agreement with Equation 1 due to an emphasis on the high k-region, that part of the experimental spectrum is typically noisier than the low-k region. The transform magnitude is a series of Gaussian shaped peaks centered about the shell radii. The heights of the peaks in the absolute value of $\phi(r)$ are related to the

9

coordination numbers for each shell and the peak widths are caused by disorder ($\sigma$) and cutoff effects due to finite data range. If we assume that the peaks are in reality delta functions, then the minimum resolution of peak width is given by $\Delta r \sim \pi/k_{max}$.

For the EXAFS data collection, which formed the bulk of this work, it was necessary to use synchrotron radiation (SR) as a source of intense, highly collimated, tunable photons. Arguments for and against using SR as opposed to a more traditional X-ray tube source can be found throughout the literature [11,13]. Each type of facility has its advantages as well as disadvantages. The high intensity, polarization, collimation and energy resolution of synchrotron radiation on an optimized beamline competes with the increased flexibility of setting experimental priorities, immediate availability to test new ideas and reduction of travel expenses offered by a laboratory system. For studies demanding maximum intensity, such as surface characterization and dilute or extremely thin sample testing, synchrotron facilities are required. For more routine analysis, however, the laboratory system allows greater adaptability to conduct proprietary or otherwise sensitive research. Due to rapid advances in SR instrumentation and apparatus during the past two decades it is feasible to collect data as good as or better than that from a tube source in a time scale improvement of approximately $10^3$. That is to say that a quality energy scan that took days to collect using a tube source can be obtained in about half an hour on a properly designed and optimized synchrotron beamline.

In any absorption experiment it is imperative that only a small fraction of the incident beam be absorbed by the initial or $I_0$ chamber. Otherwise, the photon flux impinging on the sample will be too low and may cause spurious signals and nonlinear responses in the I (transmitted, fluorescence, electron yield) detector. In practice, one accepts approximately 20% absorption [13] in the $I_0$ chamber and nearly complete absorption in the downstream chamber(s). As the detectors are gas-filled, one can control the amount of beam absorption by properly mixing the fill gases. The same absorption law which governs the sample applies to the chamber gas:

$$I = I_0 e^{-\mu x} \tag{3}$$

in which $\mu$ is the total linear absorption coefficient of the gas mixture and x is the length of the ionization chamber. It often occurs, depending on the edge energy of interest, that two gases should be mixed for optimum results. In this case, equation 3 can be written, for 20% absorption, as:

$$\frac{I}{I_0} = 0.8 = e^{-(\mu_1 f_1 + \mu_2 f_2)x} \qquad (4a)$$

$$1 = f_1 + f_2 \qquad (4b)$$

where $\mu_1$ and $\mu_2$ are the linear absorption coefficients of gas 1 and gas 2 respectively [14] at the edge of interest and $f_1$ and $f_2$ are gas weight fractions obtained by solving equations 4a and 4b.

In its most widely applied form, EXAFS is obtained by directly measuring the absorption of the photon beam as it passes through the sample; i.e., in transmission. In a transmission experiment, the absorption is given by Beer's Law, $I = I_0 e^{-\mu x}$ and the data extracted is $\mu(E)x = \ln(I_0/I)$ where $\mu(E)$ is the energy dependent linear absorption coefficient, x is the sample thickness, E is the photon energy, and $I_0$ and I are the photon intensities as measured by gas-filled ionization chambers in front of and behind the sample, respectively.

If $I_0$ is the actual incident intensity and $\zeta$ the fraction of $I_0$ that is actually measured by the detector, then $(1-\zeta)I_0$ is the signal measured in the $I_{transmitted}$ chamber, assuming the gases have been mixed to obtain total absorption in $I_{transmitted}$. The measured ratio is then $r = \zeta / (1-\zeta)e^{-\mu x}$. One wishes to maximize the accuracy in measuring changes in r due to small changes in $\mu$. Thus, $S = dr / d\mu = xr$ is the important quantity. If N is the statistical noise in r, then

$$\frac{N}{S} = \frac{1}{x\sqrt{I_0}} \left( \frac{1}{\zeta} + \frac{e^{\mu x}}{1-\zeta} \right)^{\frac{1}{2}}$$

The minimum in N/S corresponds to the maximum in S/N and occurs when $\zeta=0.24$ (about 20% absorption in $I_0$) and $\mu x=2.6$ [13]. However, it is found empirically that good statistics and clean spectra are obtained in transmission when the criterion $\Delta\mu(E)x \leq 1.5$ is satisfied [13], $\Delta\mu(E)$ being the edge jump in the absorption coefficient.

11

It has been established that detection of fluorescent X-rays, a technique well suited for thin, concentrated samples, gives the same information and can be treated by the same formalism as transmission data, with $\mu(E)=I_F/I_0$. Here $I_F$ is the measured absorption of the fluorescent X-rays by a gas-filled ion chamber.

Noise in an EXAFS experiment generally arises from four primary factors: harmonics, alignment, linearity, and offsets [15]. Each of these will be dealt with in turn. Consider the example of an absorption (transmission) experiment. If beam harmonics above the fundamental energy are present, they will be counted by both the $I_0$ and $I_{transmitted}$ ionization chambers. The presence of the sample between those two detectors attenuates each energy component differently, and since a fraction of the harmonic component photons will also be detected in the transmitted detector, distortions in the EXAFS background function will result. To minimize the effects of beam harmonics, detuning of the monochromator is sufficient as well as necessary.

If one remembers that both detectors should "see" the same beam except for the attenuation caused by the sample which is the desired effect, the problems associated with misalignment become apparent. Misalignment can approach two extremes: if the sample is smaller than the beam spot size or if other components such as sample holders unintentionally intercept the X-ray beam. These problems can be avoided by ensuring that all of the beam which passes through the $I_0$ chamber impinges on the sample and thus takes part in the absorption process. If, for example, the sample is smaller in size than the measured incident beam then a fraction of the incident beam will be counted in the $I_{transmitted}$ chamber without being attenuated by the sample. This is known as beam leakage. Similarly if there are lead "window frames" which make the effective sample area smaller than the incident beam, the ratio of $I_{transmitted}/I_0$ will be smaller than it should be due to the measured $I_0$. It is for this reason that all definition of the beam size such as by slits be made upstream of the $I_0$ chamber.

Intensity fluctuations in the beam will cancel between the detectors when taking the ratio of the signals only if they are linear, that is, if their outputs are proportional to their inputs. When using ionization chambers, this means operating them in a voltage range commonly called the

"plateau," where the output for a particular X-ray flux is independent of the actual voltage applied. Also it is important that the counting electronics be operated in their linear ranges as well. This was done by experimentally adjusting the gains and offset dark currents so that the signals measured are always much larger than the electronic noise and drift in the instruments.

One last source of noise to consider is fluctuations in the offset voltages. The offsets are the output signals produced by the detectors when the photon beam is off. The offsets were measured each time an adjustment in gain or dark current was made to any of the signal amplifiers and the data acquisition programs subtracted these offset values, which were also amplified and converted to a voltage along with the data, from the measured signals. In addition to optimizing the sample thickness, the signal-to-noise ratio can be improved primarily by two methods: averaging many scans or collecting more counts per data point by using a longer integration time.

## 2.2 XAFS Calculations

To aid in the understanding of differences in local structure due to cis or trans conformation for thiophenes, we ran calculations of XAFS data for a model consisting of a trimer with a central S atom and built the molecule as sums of coordination shells based on the monomer's structure. The XAFS calculations were performed using the program FEFF 4.08, developed at the University of Washington [16-18], and indicate that XAFS spectra should provide the structural information, as indicated by Figures 5 and 6 showing the S K-edge EXAFS function $\chi(k)$ and its $k^3$-weighted Fourier Transform, respectively, for a cis and a trans cluster of three rings each assuming planar coordination.
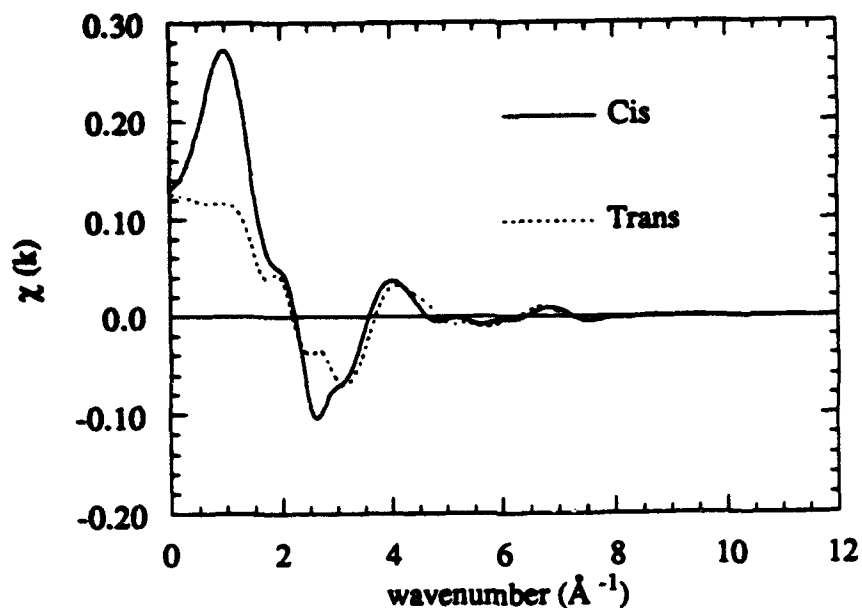
Figure 5:    Calculated $\chi(k)$ for cis and trans polythiophene
3-molecule cluster using the program FEFF.
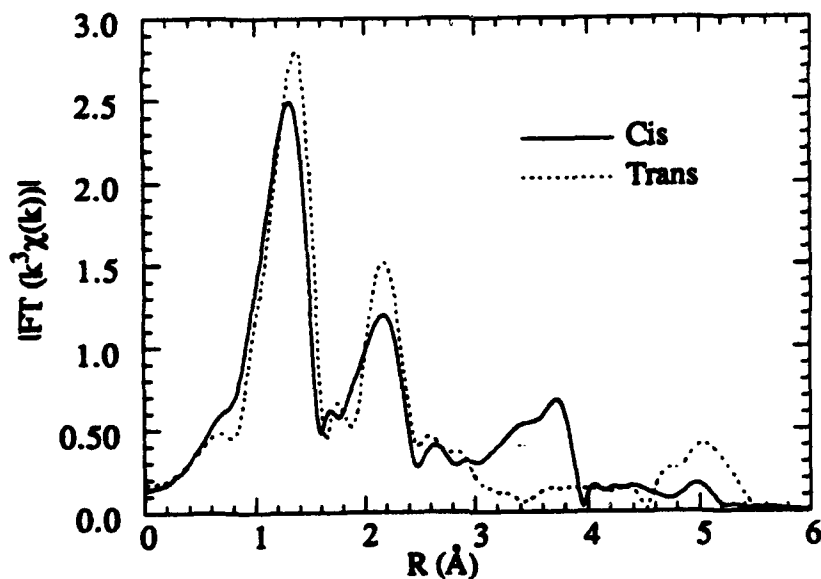


Figure 6:    $|FT\ (k^3\chi(k))|$ for cis and trans polythiophene
3-molecule cluster from the $\chi(k)$ functions
generated using FEFF from Figure 5.

Most of the $\chi(k)$ information comes from the near edge region, since S is a weak scatterer. Thus,

the shape of the near-edge region will provide information on cis or trans characteristics. The first

14

two main peaks in the FTs of Figure 6 correspond to the two S-C coordination shells, which should be similar, and the marked difference in the S-S nearest neighbor (in the next thiophene ring) peak position shows how cis and trans differ in sulfur coordination using crystallographic data [19] as a model.

The theoretical radial distribution function [19] for the Br end cap in 2,5-dibromothiophene is shown in Figure 7, and the FEFF-calculated $\chi$ function and the magnitude of its $k^3$ weighted Fourier transform for that distribution in Figures 8 and 9. It should be noted that this is really a "linear distribution" function since the Br is not symmetrically distributed within the molecule, in a manner analogous to the Cl-substituted system shown in Figure 1.
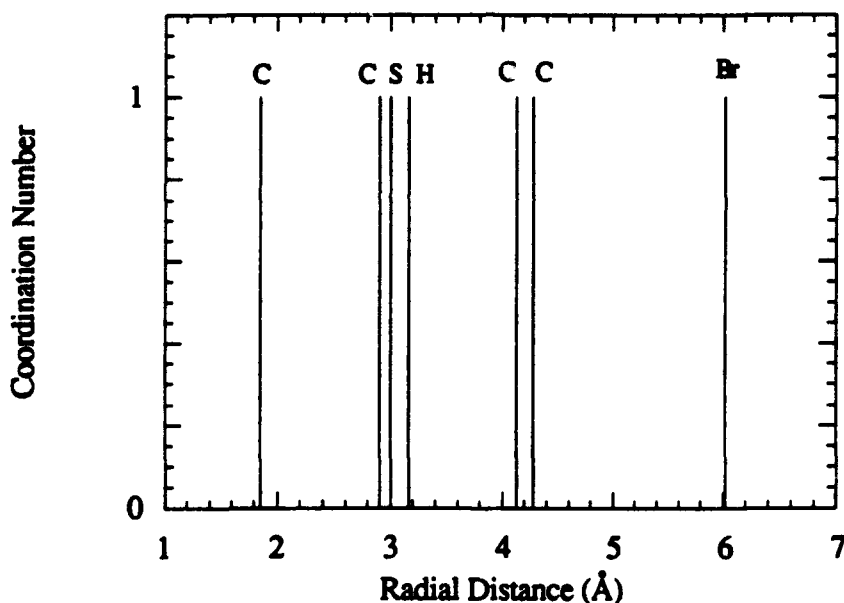
Figure 7: Radial distribution function for Br in 2,5 dibromothiophene monomer. The individual atomic species are shown above their respective δ function peaks. Calculated from reference [19].
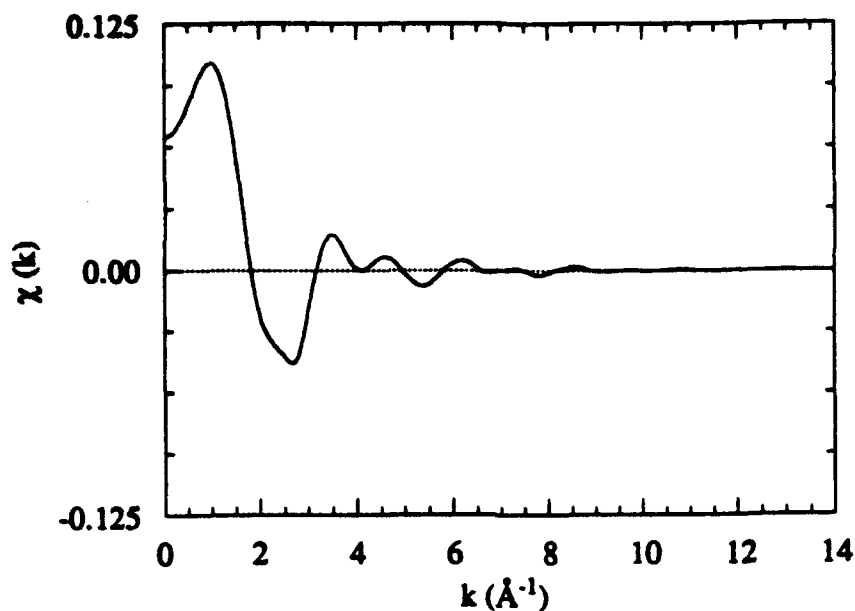
Figure 8:     FEFF-calculated Br K-edge $\chi$ (k) vs photoelectron
              wavenumber k in Å$^{-1}$ for 2,5 dibromothiophene.
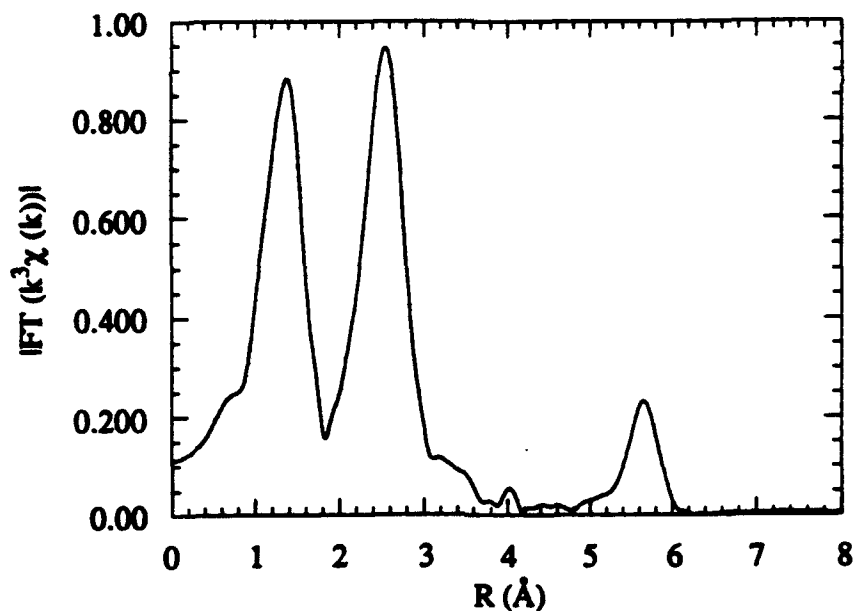


Figure 9:     IFT (k$^3\chi$ (k))I vs radial distance R in Å for the Br K-edge in
              2,5 dibromothiophene using the $\chi$ calculated by FEFF.

The curve in Figure 9 is known as the "radial structure function" rather than a true radial

distribution function [20] with peaks corresponding to scattering from atoms located at each

16

scattering distance $R_i - \alpha$. The factor $\alpha$ is due to the effect of the phase shift which was not included in the transform, since it is an unknown quantity.

As developed in Section 2.1, the resolution of features in R-space will depend on the quality of the data at the high end of the k-space range. In a pure cis system (planar), the S-S nearest neighbor distance is calculated from the crystal structure to be 4.01 Å and for a pure trans system (planar) is 5.51 Å, so the data range becomes a concern in determining sensitivity to these differences. The calculated curves shown in Figures 5 and 6 are for "perfect" conditions: pure phases and data extending out to 20 Å⁻¹. The $\chi$ and FT($\chi$) functions for the two phases were modeled for a variety of k-ranges. Figure 10 illustrates the effect on the magnitude of the FT of limiting the k range to 12.55 Å⁻¹ for trans and 12.70 Å⁻¹ for cis (endpoints coincide with nodes in $\chi(k)$) respectively. A typical data scan for these materials extends cleanly to about 12 Å⁻¹.
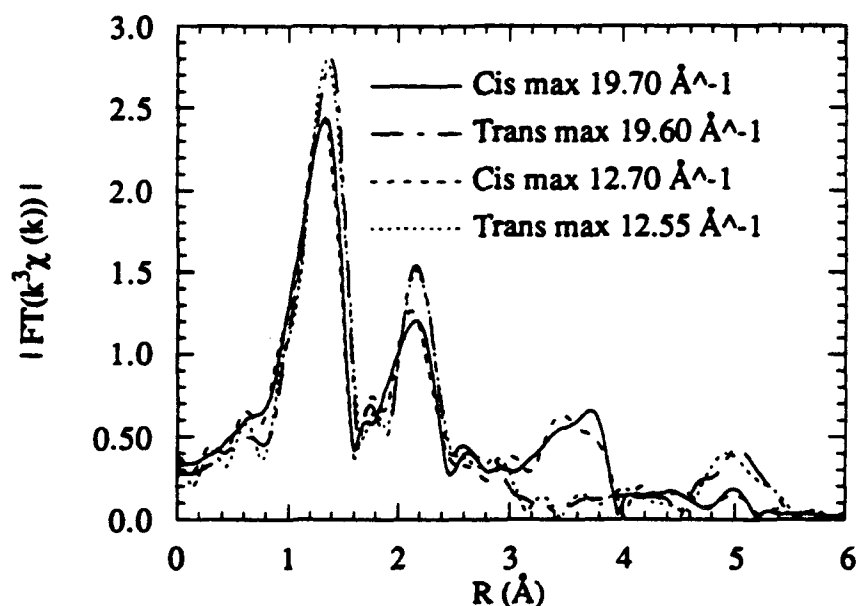


Figure 10:  Overplot of FT magnitudes for two different k-ranges in cis and trans tri (thiophene) S K-edge EXAFS. The values given with the line shapes are the $k_{max}$ for the FTs.

Table 1 lists the peak positions and magnitudes for the first 3 FT peaks for 4 terminal k values modeled.

**Table 1:** FT peak positions $R_i$ and magnitudes for cis and Trans trithiophenes calculated using FEFF.

| Material | k range ($\text{Å}^{-1}$) | $R_1$ ($\text{Å}$) | Magnitude | $R_2$ ($\text{Å}$) | Magnitude | $R_3$ ($\text{Å}$) | Magnitude |
|---|---|---|---|---|---|---|---|
| Cis | 2.25-19.70 | 1.34 | 2.44 | 2.16 | 1.21 | 3.72 | 0.66 |
| | 2.25-12.70 | 1.30 | 2.49 | 2.12 | 1.27 | 3.46 | 0.63 |
| | 2.25-9.75 | 1.22 | 2.26 | 2.00 | 1.12 | 3.32 | 0.51 |
| | 2.25-8.45 | 1.20 | 2.09 | 2.02 | 1.17 | 3.24 | 0.51 |
| Trans | 2.20-19.60 | 1.38 | 2.80 | 2.16 | 1.54 | 5.02 | 0.43 |
| | 2.20-12.55 | 1.34 | 2.79 | 2.16 | 1.51 | 4.94 | 0.40 |
| | 2.20-9.95 | 1.28 | 2.33 | 2.24 | 1.10 | 4.90 | 0.32 |
| | 2.20-8.70 | 1.34 | 2.26 | 2.20 | 1.03 | 4.84 | 0.24 |

Since the data in Figure 10 and Table 1 do not indicate any overlap between the third shells even at $\Delta k \sim 6 \text{Å}^{-1}$ and the full width of the peaks is $\Delta R \sim 2\pi/\Delta k$ which for two peaks 1.5 Å apart would correspond to a k-space width of 4.19 $\text{Å}^{-1}$, it can be concluded that the pure phases should be distinguishable from EXAFS $\chi$ data extending to 12 $\text{Å}^{-1}$. Furthermore, the short range order results can be used for verification of various structural models built using molecular modeling techniques [21].
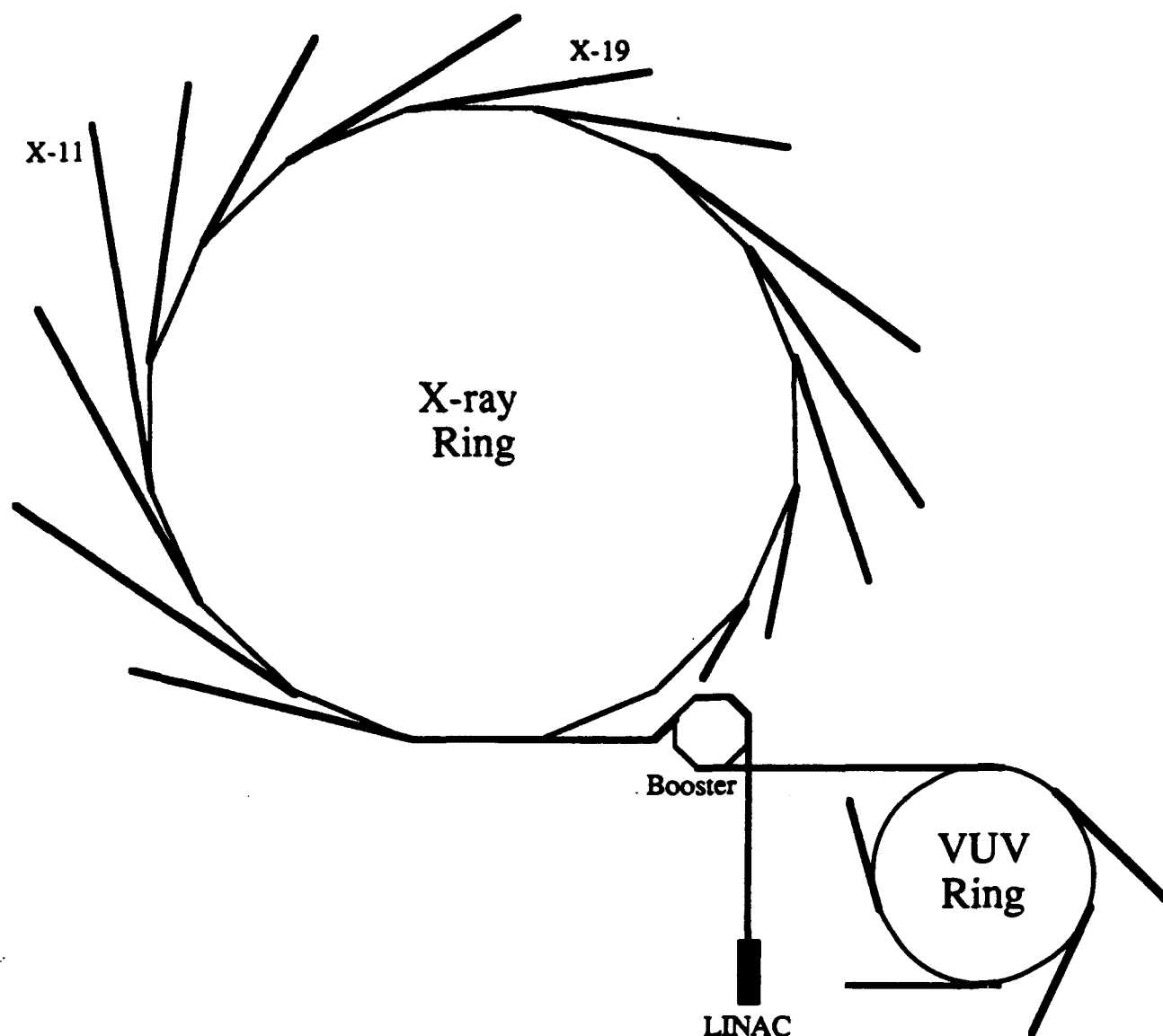
**Figure 11:** Partial floor plan of the National Synchrotron Light Source experimental area. The circumference of the X-ray Ring is 170.1 m and that of the Vacuum UltraViolet (VUV) Ring is 51.0 m. For clarity, only a few of the actual number of beam ports are shown here. There are 30 beamports on dipoles and 5 insertion devices on the X-ray Ring and 17 beam ports on dipoles and 2 insertion devices on the VUV Ring. Maximum current on the X-ray Ring is ~250 mA at 2.5 GeV stored electron energy and a typical lifetime is 20 hours.

### 3.3.1.1    Beamline X-11A

Bromine K-edge data ($E_0$ = 13474 eV) were obtained on beamline X-11A in both fluorescence yield and transmission modes. This beamline was available to the experimental team

21

since one of its members is also a member of the beamline's Participating Research Team (PRT). Since these were the initial experiments, the high flux, good tunability, and general ease of operation at higher energies due to reduction of air absorption were taken advantage of on this line. While this beamline has been described in great detail in the literature [22-24], its major features will be pointed out here as well. When a particle of charge z is accelerated it will radiate. At low (nonrelativistic) energies the radiation field is characterized as a dipole as illustrated in Figure 12 (a):



(a)                                 (b)

Figure 12:    Schematic drawing of radiation field distribution for a
nonrelativistic (a) and relativistic ($\gamma \gg 1$) (b) charged
particle due to acceleration.

As the particle approaches the speed of light, the radiation field distribution will peak in the direction tangential to the local radius of curvature with angular distribution on the order $1/\gamma$ where $\gamma = E_{particle} / mc^2$, as indicated by Figure 12 (b). Synchrotron radiation is produced by bending a beam of ultra-relativistic electrons [25] of approximately 2.5 GeV energy by the use of a dipole magnet. This radiation then passes down an evacuated beam pipe and into the sample hutch. On its way it traverses a photoelectron beam monitor, a Be window to isolate the beamline from the main synchrotron ring vacuum, a SiC collimating mirror which was not used in these experiments, another Be window, a beam position monitor and slits to define the beam entering the monochromator, the 2- or 4-crystal monochromator which is used to tune the energy of the X-rays, a photon shutter to isolate the experimental hutch from the incident beam, a set of horizontal and vertical slits to define the size of the beam on the sample, an incident ionization chamber, and then into the sample-holding cell. A diagram of beamline X-11A is shown in Figure 13, illustrating the major components of that facility.

22
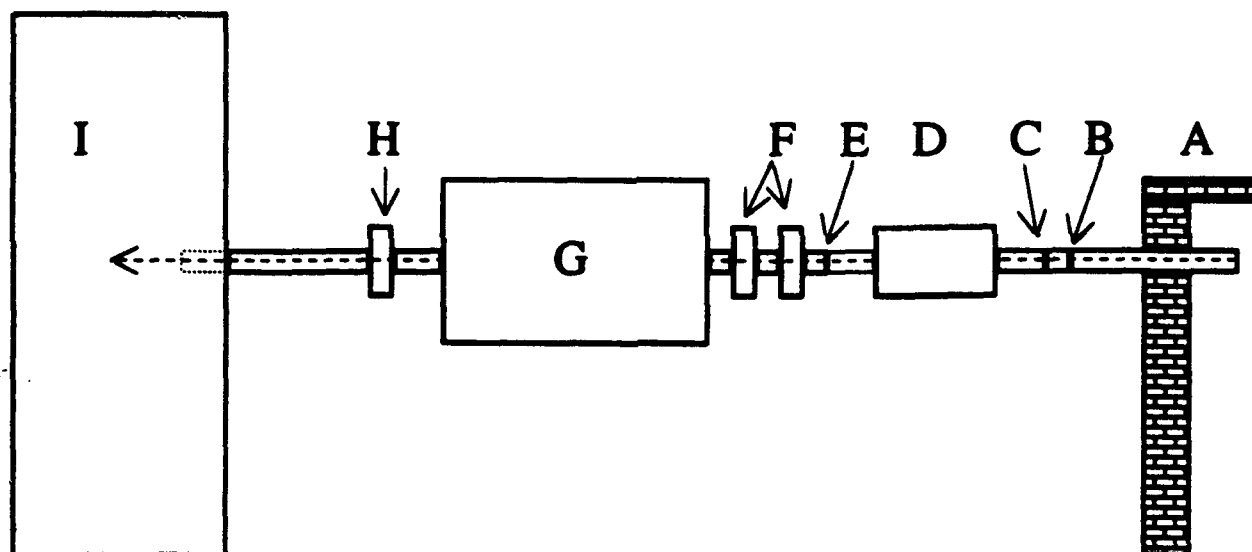
Figure 13:    Block diagram of a typical synchrotron beamline. Reading from right to left (beam direction) is A) concrete shielding, B) photoelectron beam monitor, C) Be window, D) SiC mirror for collimation, E) Be window, F) beam monitor and slits, G) monochromator, H) photon shutter, I) experimental hutch. The dashed arrow indicates the X-ray beam direction. Adapted from reference [23].

The monochromator used in this beamline is somewhat unique. It can be used in either a two or four crystal mode which allows optimization of the intensity and/or the resolution for a particular experiment. For this work, the two crystal geometry was used with a pair of Si (111) crystals to tune the beam energy. The pair of crystals was mounted on a Huber 421 goniometer with piezoelectric adjusters for fine tuning the parallelism of the pair. The crystal assembly is mounted in a vacuum tank which operates at approximately $10^{-5}$ Torr. The angular range of this monochromator is 5° - 35° which gives an energy range of 3.5 - 22 KeV with Si (111) crystals. For a 0.5 mm slit opening upstream of the monochromator, the two crystal configuration has an energy resolution of ~ 2.7 eV at the Cu K-edge (8979 eV) [23]. The two crystal mode of operation is called non-dispersive since an incoming ray which deviates from the central ray at $\theta$ by $\Delta\theta$ on the first crystal will also have the same deviation at the second, with parallel crystals as shown in Figure 14.
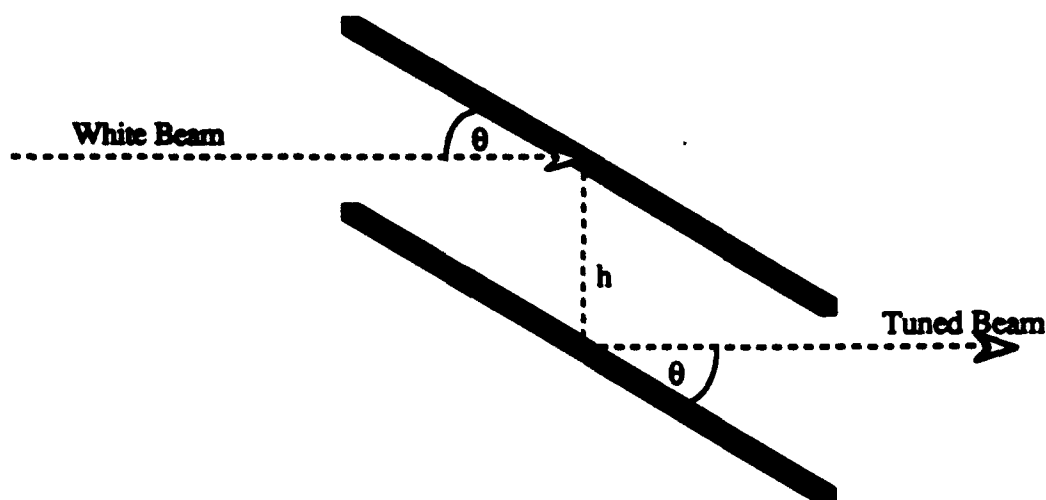
Figure 14:    Nondispersive configuration of a two crystal monochromator.
            The energy resolution of the pair (assuming perfect crystals)
            is a function of the source size and slits used in the beamline.

The output beam emerges parallel to the incident beam with an offset given by $h=2d\cos\theta$, where d is the crystal interplanar spacing. As the height difference depends on the angle $\theta$ and thus the emitted photon energy, vertical translation of the sample as a function of photon energy is required during a scan to maintain alignment. To reject higher order harmonics from the incident beam, which would simply look like a large "dc offset" in the $I_0$ chamber [26] and reduce signal-to-noise considerably, a detuning capability has been built into this monochromator, as well as most, to adjust the crystal pair to be slightly non-parallel. These higher energy harmonics ($\lambda/n$ where n is an integer and $\lambda=2d\sin\theta_B$) are narrower in energy than the fundamental and thus are removed without causing significant loss in fundamental intensity. Typically, 15-25% detuning, i.e., a reduction of the signal measured in the $I_0$ chamber by 15-25%, of $I_0$ at 50-100 eV above the absorption edge under investigation is found to provide good signal-to-noise near the Br K-edge ($E_0$=13474 eV) on X-11A.

In the non-dispersive configuration all the incident rays are reflected since they all impinge at angle $\theta$ [13]. This means that the energy resolution of the pair is determined by the source size and the upstream beamline slits. Water cooling of the first crystal was used to reduce parallelism

errors and lattice spacing mismatch caused by thermal expansion induced by the large heat load of the incident white beam.

The $I_0$, $I_{transmitted}$, and $I_{reference}$ ionization chambers, as well as an X-Z table for holding samples / detectors are mounted on an optical rail which is in turn attached to a standard Newport breadboard table. To maintain alignment, the table height is varied by the use of an automatic feedback system under computer control. The current signals from the various detectors are amplified and converted to a proportional voltage by a set of Keithley Model 427 / 428 current amplifiers. The voltage outputs from these amplifiers are then measured by a voltage-to-frequency converter which is interfaced to the beamline computer via a CAMAC crate. Beamline control operations are achieved by an IBM PS/2 computer running OS/2. This system allows interactive data analysis up to preliminary isolation of $\chi$, setting up and executing scan parameters, and complete control of beamline operations other than opening/closing photon or safety shutters.

### 3.3.1.2 Beamline X-19A

For the Cl and S K-edges (2823 and 2474 eV, respectively) beamline X-19A was used in the General User (external, non-PRT member) mode of operation, since it is optimized for those energy regions. Beamline X-19A is also of a "typical" XAS design whose construction differs from that of X-11A primarily in its monochromator design. Synchrotron radiation emerges from the storage ring into a standard NSLS front end, which is the interface between the storage ring and the beamline vacuum systems, similar to X-11A and passes through a white-beam slit which is used to limit the vertical divergence, exclude scattered radiation and control the heat load on the first monochromator crystal. The X-rays then pass through a white-beam monitor, which detects photoelectrons emitted by a 90% transmitting W mesh. This forms part of the beamline feedback circuit. From there the radiation enters the "NSLS boomerang-type" monochromator [27] which is a non-dispersive pair but which differs from the X-11A design in that the beam emerges at constant height independent of photon energy. The emergent beam is sampled by a channel electronic multiplier monitor. Downstream is an available cylindrical aluminum refocussing mirror, which was not used, and photon shutter and slit assemblies. The entire beamline is maintained at ultra

25

high vacuum ( approximately $10^{-10}$ Torr ) up to the 10 mil thick Be window inside the hutch, which minimizes intensity losses from air which are common in this energy range. Experimental detectors and amplifiers are quite similar to those used on X-11A, and the beamline is controlled by a DEC MicroVAX II computer running Micro-VMS interfaced through a CAMAC crate.

With Si(111) crystals, a Bragg angular range of 14.5° to 70.0° corresponds to tunable energy of 2.12-7.93 KeV. For the same reasons as presented above, detuning of the crystal pair is required to reduce harmonic contamination of the fundamental beam. At the lower energies available on this line, detuning by 70% was used. Even with water cooling a significant heat load on the first crystal still exists. The heat load and detuning problems require continuous angular correction to maintain energy calibration as well as fixed output position. This correction is achieved by a piezoelectric feedback system used to fine tune the angle of the second crystal. This analog system is based on one described elsewhere [28] in the literature. It monitors the efficiency of the monochromator by forming the ratio of a signal proportional to the white beam flux and one proportional to the monochromator output flux [29]. The feedback system keeps this ratio equal to a reference signal. The energy resolution of this beamline is reported to be approximately 0.7 eV at 3 KeV with a 2.0 mm slit opening and Si (111) crystals [29].

The sample chamber consisted of a standard Lytle detector with gas inlets and outlets to allow purging of air from the volume surrounding the sample. This is not important when dealing with 13 KeV X-rays around the Br K-edge, but for very soft radiation near Cl and especially S, air path minimization is essential to reduce losses in beam intensity due to absorption by the air. To allow maximum use of available photons by minimizing the amount of time required to purge the sample chamber at the soft edges, a multi-sample holder was designed and built [30] to allow selection of any of five samples by means of a pulley and string fed through the lid of the sample chamber. Thus, five samples could be loaded all at once and the sample chamber purged for a single 10-15 minute (see Section 5.3.1) period only once per 6 hours. The experimental setup is shown in Figure 15, and the revolver/sample holder is shown in Figure 16.
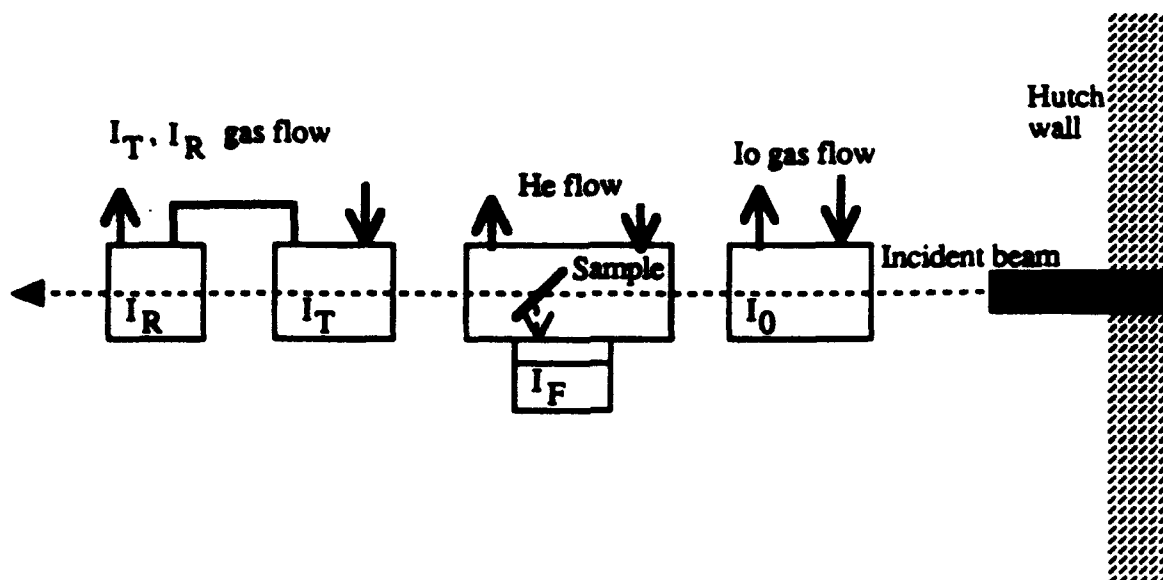
**Figure 15:** Top view of experimental setup inside the beamline hutch. The sample can be held at 45° or normal incidence with respect to the X-ray beam. Windows of Kapton™ or Mylar™ placed on the up- and downstream ends of the detectors allow the X-rays to enter and exit essentially unattenuated by those windows.
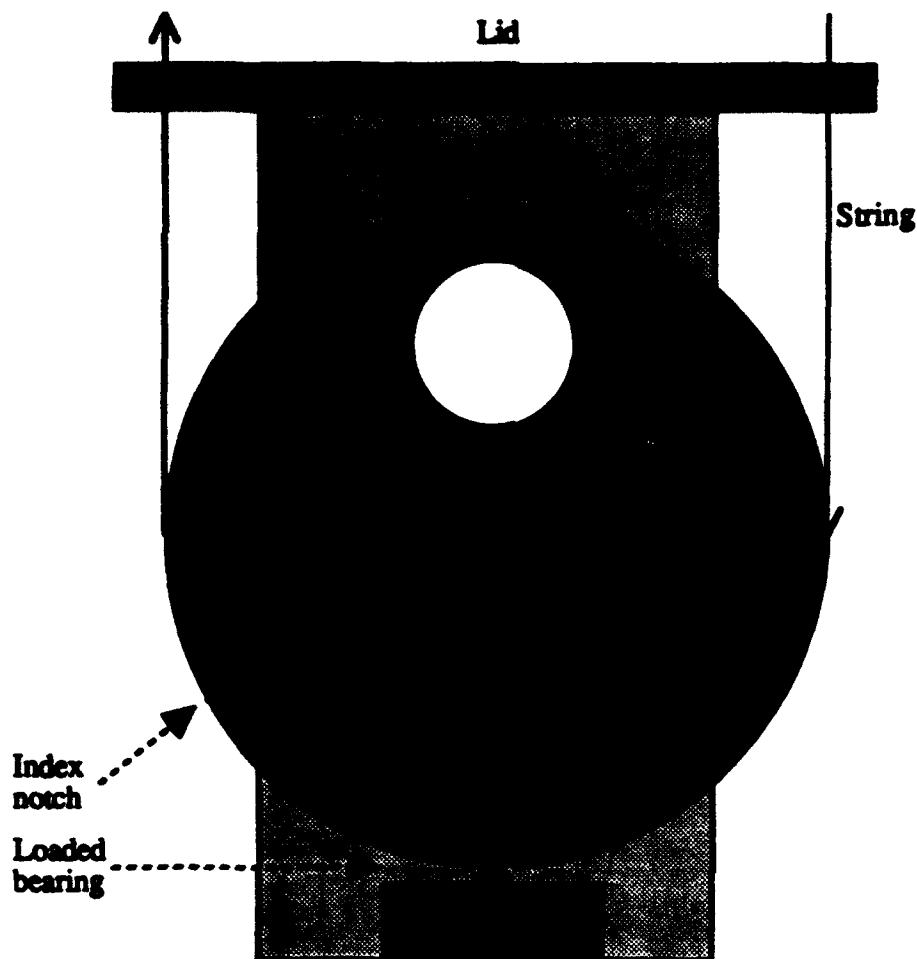
Figure 16:    Revolving magazine-type sample holder. There are five positions where samples can be simultaneously mounted with clear-through holes behind them. The large hole at the top is for rough initial alignment of the detector, and the entire unit screws into the lid of the sample chamber at either 45° or normal incidence to the X-ray beam.

For both beamlines, the NSLS X-ray ring was operating at an electron beam energy of 2.5 GeV with a stored current of 110 to 140 mA on X-11A, 120-200 mA for Cl edge on X-19A, and 200-240 mA for S edge on X-19A. Most of the data on X-11A were collected using a 2 second integration time in the EXAFS region and two scans for each sample. The Cl and S data on X-19A were collected in two scans using the integration times in Table 3. A full EXAFS spectrum over the range -200 eV to +1000 eV with respect to $E_0$ is accomplished in approximately 30 minutes on both beamlines. Transmission and fluorescence modes were both used to collect the Br K-edge data on beamline X-11A. Gas-filled ionization chambers were used with a mixture of 85% $N_2$ to

28

15% argon by volume in $I_0$, pure argon in $I_{transmitted}$, and pure Kr (static) in $I_f$ for the Br K-edge at X-11A. On X-19A, $I_0$ was filled with pure flowing He, $I_{transmitted}$ with 25% $N_2$ and 75% He by volume, and pure $N_2$ (static) in $I_f$ since we were not measuring $I_f$. The sample chamber was flushed with flowing He at a rate of 1 liter/min to minimize absorption by air for the Cl and S edges on X-19A. An $I_{reference}$ chamber was used on X-11A and the gas flow was connected in series with the $I_{transmitted}$ chamber such that the outlet of the $I_{transmitted}$ chamber served as the input for the $I_{reference}$ chamber. A $KBrO_3$ pellet was used as a reference for the Br edge.

### 3.3.2 EXAFS Data Collection Parameters

The computer systems on both beamlines allow the user to completely specify the parameters to be used while collecting data. They differ mainly in their syntactical structure since the two scan programs are different. The scan energy ranges on X-11A are all relative to $E_0$ so when going from one absorption edge to another the scan definition remains the same, independent of what value $E_0$ is assigned. The X-19A program requires absolute energy values to define regional boundaries. This constraint necessitates a completely different scan definition for each absorption edge. Parameters for a standard full EXAFS scan on X-11A are given in Table 2 and a full EXAFS scan at the Cl K-edge on X-19A in Table 3. Data file names are assigned when starting a scan on X-11A while they appear in the scan definition file in the X-19A system.

Table 2:    Scan parameters for use on beamline X-11A. All energies and
            wave numbers are relative to $E_0$, which is arbitrary in the scan definition.

| Region | Lower Bound | Upper Bound | Step Size | Integration Time (sec) |
|--------|-------------|-------------|-----------|------------------------|
| 1 | -200 eV | -50 eV | 10 eV | 1 |
| 2 | -50 eV | 50 eV | 1.0 eV | 2 |
| 3 | 50 eV | 16 Å⁻¹ | 0.05 Å⁻¹ | 2 |

**Table 3:** Scan parameters for Cl on beamline X-19A. The k-space ($Å^{-1}$) definitions are based on $E_0 = 2.822$ keV, which was input to the scan definition file.

| Region | Lower bound | Upper bound | Step size | Integration Time (sec) |
|--------|-------------|-------------|-----------|------------------------|
| 1 | 2.622 keV | 2.772 keV | 10 eV | 4 |
| 2 | 2.772 keV | 2.872 keV | 0.5 eV | 4 |
| 3 | 2.872 keV | 16 $Å^{-1}$ | 0.05 $Å^{-1}$ | 4 |

The sulfur data were experimentally difficult to measure due primarily to the two facts that S is very close to the low energy end of beamline X-19A's capability and that air absorption is a major factor for S as well as Cl, even when the sample chamber is flushed with He. Two primary factors also limit the range of data obtainable from a practical point of view. The first is that the argon K-edge is at 3205.9 eV, which is 383.9 and 783.9 eV above the Cl and S edges, respectively. The second limiting factor is related to the first in that commercial grade He gas contains argon as an impurity, however small, but there will always be a contribution from argon, even when all the air (which also is known to contain argon) is flushed from the sample chamber with He. The low levels of argon from this source should not be observable in transmission, but could pose a problem in fluorescence. According to the equation relating energy and wave number given in Section 2, the position of the argon edge with respect to the Cl and S edges necessitates truncation of the $\chi$ data at 10.06 and 14.39 $Å^{-1}$, respectively. To remove this limitation, an evacuated sample chamber would be required. Another possible source of argon comes from the way in which the thin films were deposited. Since an argon plasma was used in the PECVD process, an unknown quantity of argon may be trapped in the film samples. With the above listed limitations, these XAFS observations alone cannot unambiguously tell the story of argon trapped in the films from deposition. All other factors being equal, such as purge time and He flow rate during XAFS measurement, an analysis of argon edge height, as outlined below, could provide a measure of relative amounts of argon in the samples.

It was independently observed that the argon level reached its base value in 10-15 minutes after closing the sample chamber shown in Figure 15 and purging with He gas by monitoring the $I_{transmitted}$ signal at a fixed energy. In other words, after 10-15 minutes, $I_{transmitted}$ reached a steady value. As was shown in Figure 16 the samples were mounted on a revolving disk. This allowed indexing between samples without having to open the sample chamber. As a result, all of the edge information presented in Table 5 was collected after $I_{transmitted}$ reached its steady value, since each scan took 20-30 minutes.

# Section 4

# DATA ANALYSIS

The procedure used here can be divided into two main parts. The first includes initialization and background removal to obtain normalized EXAFS oscillations. This normalized data can then be analyzed by the theory developed in Section 2. The second major step in the analysis extracts the parameters of interest. The analyst has several tools at his disposal for this part of the procedure. These include Fourier transform (FT) and Fourier filtering of single shells, direct comparison of EXAFS ($\chi$) spectra, isolation of single shells, and curve fitting or calculation.

## 4.1 Preliminary Analysis

### 4.1.1 Initialization

The programs used in this study to analyze the EXAFS data are FORTRAN codes developed primarily at the University of Eindhoven with modifications at the Naval Research Laboratory and Naval Surface Warfare Center over the course of about a decade. The underlying philosophy is that interactive graphical analysis is crucial to allow examination of the effects of each mathematical manipulation of the data. They enable one to analyze data collected from many different beamlines / synchrotron facilities by putting the data into a standard format. After the raw data have been initialized, the analysis proceeds without regard to the origin of the particular data set. A full XAFS spectrum for 2,5 dibromothiophene monomer at the Br K-edge collected in transmission is shown in Figure 17.

33
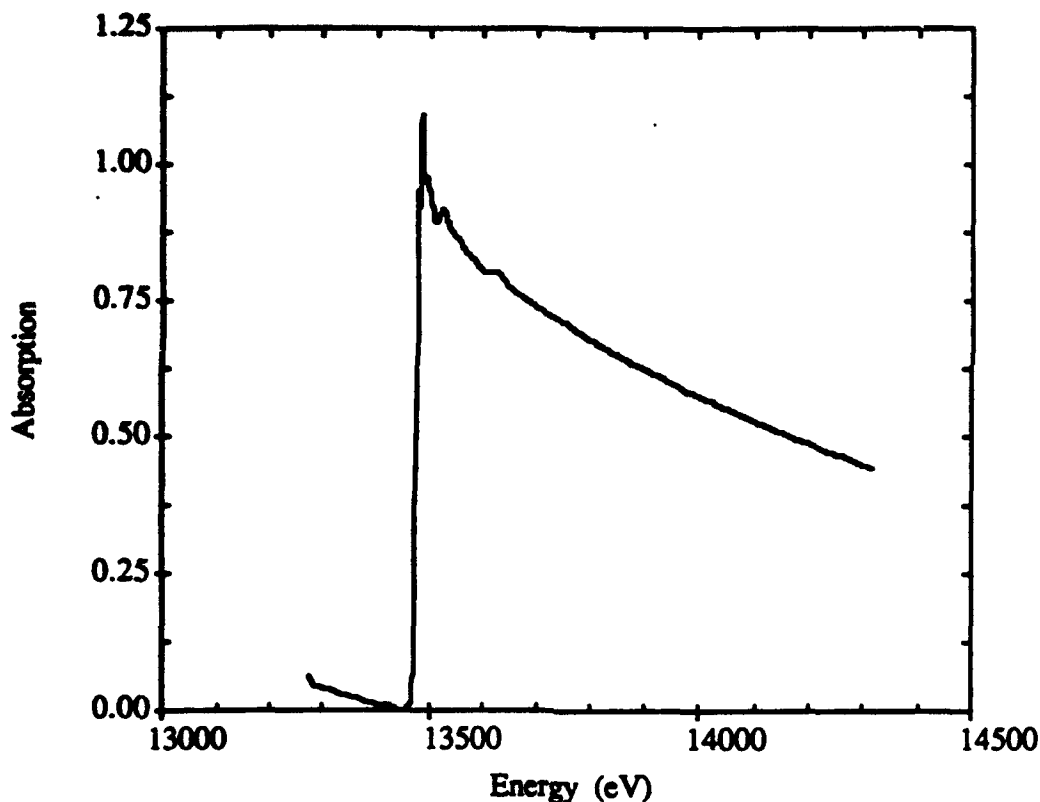
Figure 17:   Full XAFS spectrum for 2,5 dibromothiophene monomer
collected in transmission mode at the Br K-edge. Four
scans were averaged.

### 4.1.2 Pre-Edge Subtraction

Below the absorption edge of interest, the measured background contains contributions from several sources, such as Compton scattering and other (lower energy) absorption edges if present. It is useful, especially for near-edge studies, to remove this pre-edge background. This is done by fitting the data below the edge to a suitable function. In general this pre-edge is fitted to the "Victoreen" function [31]:

$$\mu x = \frac{A}{E^3} - \frac{B}{E^4} \tag{5}$$

where E is the incident photon energy and A and B are determined from the least squares fit. It is found in practice that for transmission data a quadratic pre-edge function is a good approximation, and for fluorescence even a linear function will suffice [32]. Usually this curve is fit between two points in the data set; the first "good" point and the point at which the absorption edge begins to

34

occur. The first point in the pre-edge fit is determined from visually examining the data, and is usually the first point in the data file unless the acquisition program began to collect data before ramp down of the monochromator and settling of detectors was completed. In the case of computer error, the second point in the file is taken as the first point in the pre-edge fit. Also, if the sample contains more than one distinct absorption edge in the energy range of the scan, one may select which edge to use in the analysis by proper choice of pre-edge limits. Figure 18 shows the quadratic pre-edge function which is to be subtracted from the data of Figure 17 and the data itself.



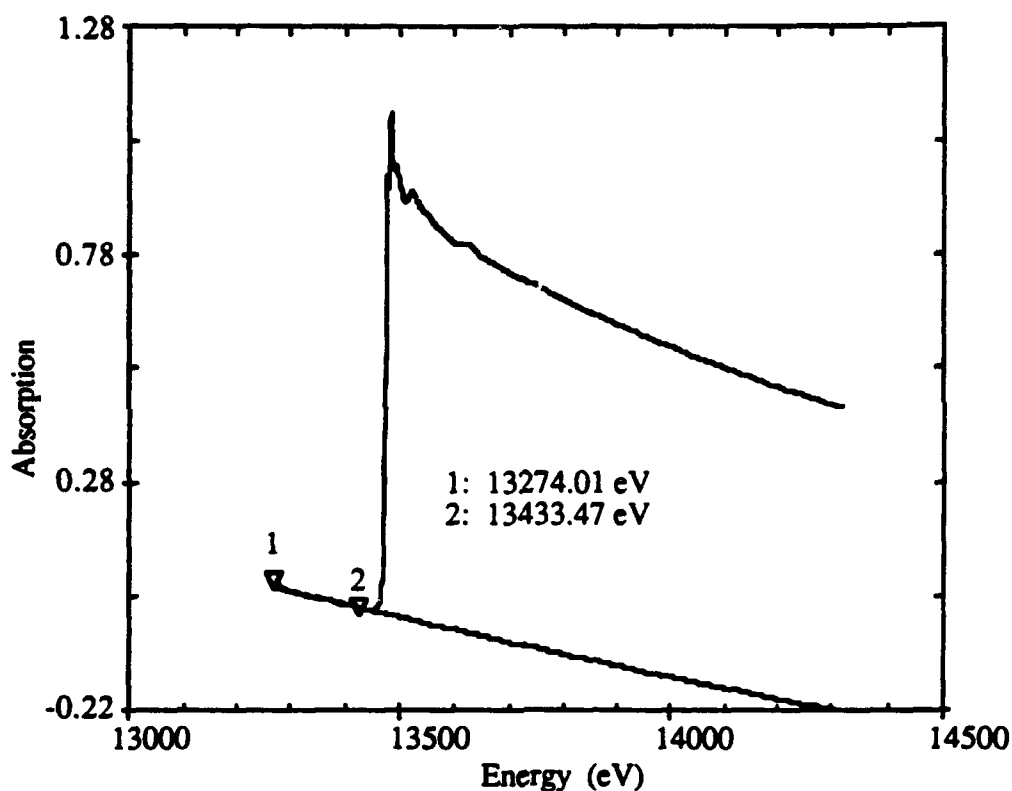Figure 18: XAFS spectrum and quadratic pre-edge function for 2,5 dibromothiophene monomer collected in transmission mode at the Br K-edge. The two points for the least-squares fit to the pre-edge are shown on the graph.

It is possible for the analyst to specify both of these points. This is especially useful when comparing several spectra at the same edge to provide consistency in the analysis.

### 4.1.3 Edge Energy Determination

Even though the EXAFS technique is relatively insensitive to the absolute energy calibration of the monochromator it is useful, again to maintain consistency, to define an energy threshold $E_0$. This is done by mathematically determining the inflection point in the absorption edge spectrum. When analyzing materials with similar chemical or crystallographic compositions the same $E_0$ value should be used for the entire group. Therefore, one lets the program mathematically determine the threshold energy of the "pure" sample, and then manually assigns that number for $E_0$ to subsequent samples to maintain consistency. For 2,5 dibromothiophene monomer at the Br K-edge, this point is taken as the inflection point roughly one-third of the way up the edge jump, as shown in Figure 19.
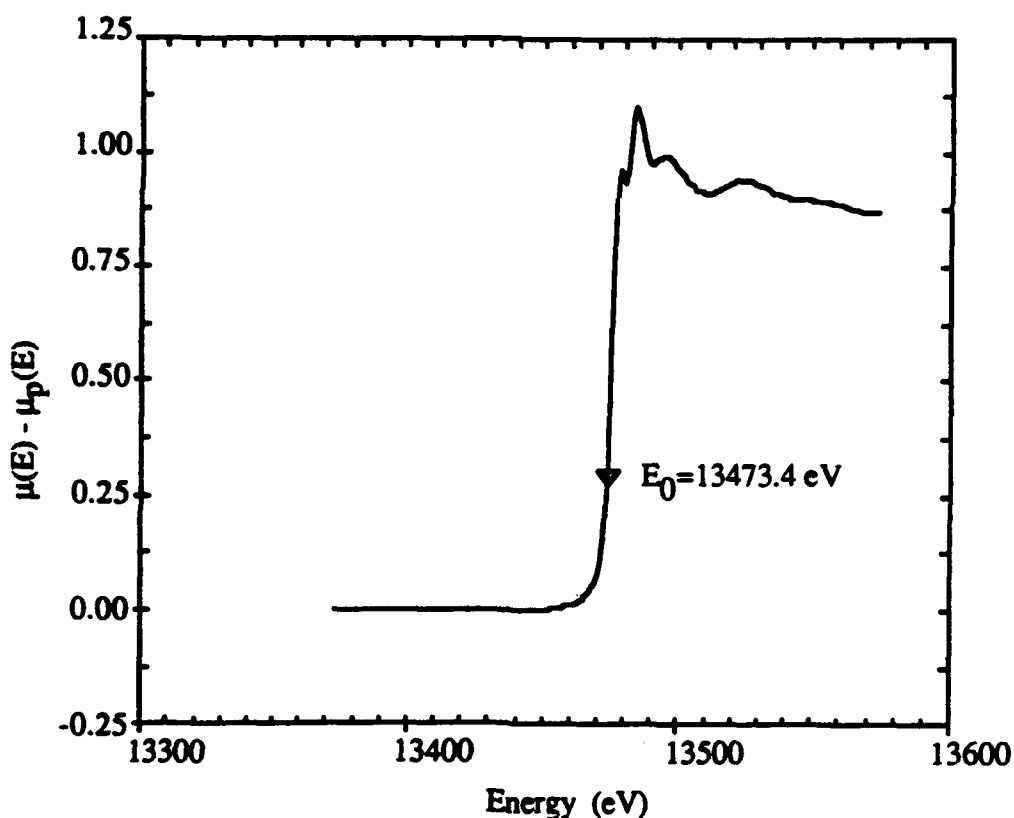
Figure 19:   Br K-edge X-ray absorption Near Edge Structure
for 2,5 dibromothiophene collected in transmission.

Figure 20 illustrates the pre-edge subtracted, energy scaled to the absorption edge, data from which $\chi$ will be extracted.

36
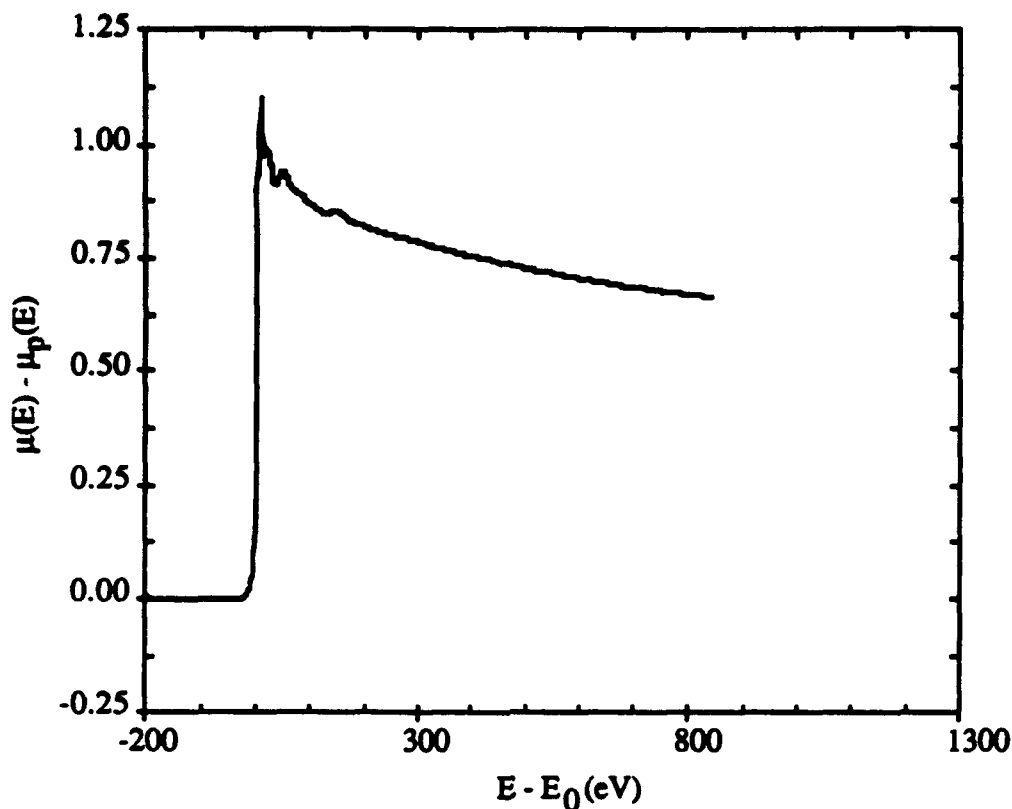
Figure 20:   Br K-edge transmission spectrum of 2,5 dibromo-
thiophene monomer with quadratic pre-edge function
subtracted. $E_0 = 13473.4$ eV

## 4.1.4 Background Removal

The background above the edge is more complex than that below it and thus must be carefully removed in order to properly normalize the data and later extract structural parameters. There are several methods for determining the post-edge background function, and in this work the background is obtained as a cubic smoothing-spline approximant to the data [33]. This method, as well as the several others in wide use today, depends on the background being slowly varying with respect to the EXAFS oscillations.

Two parameters may be varied by the user: one determines the "tightness" of fit and the other is an inverse weighting parameter. The procedure is to treat the independent variable of each data point as a knot of the spline function. The corresponding data set $Y_i$ and a set of inverse weighting factors $W_i$ are used to construct a set of spline coefficients $S_i$ such that

$$SM > \sum_i \left( \frac{Y_i - S_i}{W_i} \right)^2. \tag{6}$$

The parameter SM, which is supplied by the analyst, determines the tightness of the fit and the sum is over the data points. The fitting routine then constructs the curve with the lowest average curvature. In practice the first inverse weighting parameter $W_1$ is held fixed at a small value to force the spline to go through the first data point and the tightness parameter is varied, although there are argument  or allowing $W_i$ to vary with k [34]. This tightness parameter is varied by an iterative process by which one examines the FT and background derivative. Using a tightness parameter that is too small will cause non-physical peaks in the FT at small radial distance while if too large a value is used, the oscillations in the background derivative will too closely follow those of the EXAFS and the amplitudes of the FT peaks will be reduced.

The standard procedure is to visually compare plots of the FT and background derivative and determine what final value to use for the smoothing parameter. Also important is the k-range used in the FT. Usually, one specifies the k-range to start with the first zero of $\chi(k)$ and extend to a k-value dependent on the quality of the high-k data. Plots showing the effect of smoothing parameter on the FT and background derivative are shown in Figures 21 and 22 for various SM values. Note that while the FTs in Figure 21 were calculated over the range 0 - 8 Å, only the region from 0 - 4 Å is shown here to emphasize the effect of changing SM on the low - R region of the spectrum.
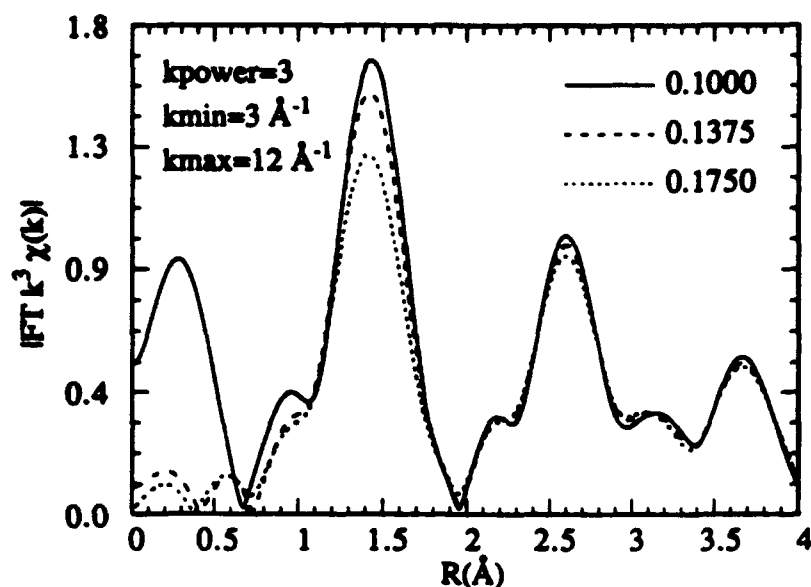
Figure 21: Fourier Transform Magnitude vs radial distance in Å
for 2,5 dibromothiophene as a function of tightness
- of - fit parameter SM.
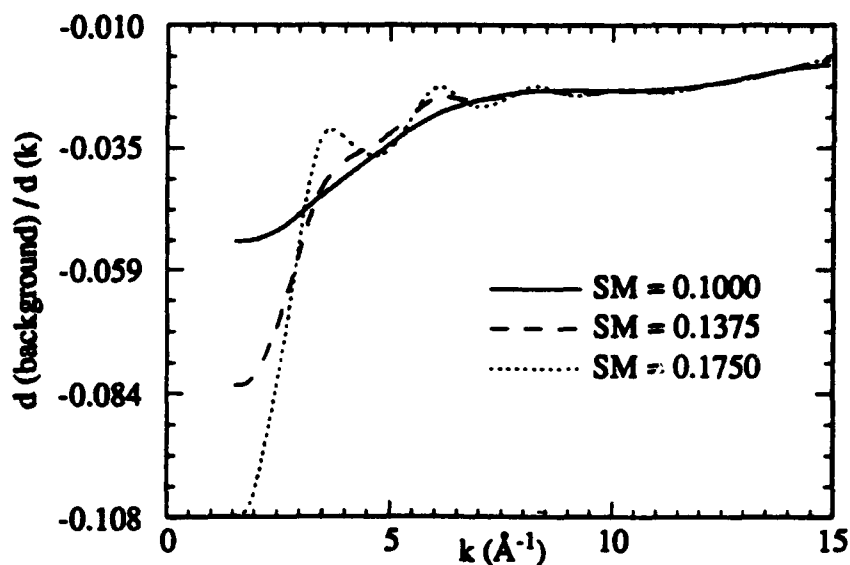


Figure 22: Post-edge background derivative vs photoelectron
wave number k in Å⁻¹ for 2,5 dibromothiophene
monomer as a function of SM.

Notice how small changes in SM affect the low-R region of the FT magnitude. For SM = 0.1000

the FT has large amplitude at low R and the background derivative is very smooth, but by the time

SM increases to 0.1750 the main peak has begun to decrease significantly. As seen in Figure 22

39

the background derivative oscillations have increased a great deal for SM=0.175 compared to SM=0.1375. If the frequency of the oscillations in the background derivative too closely approaches that of the EXAFS, then the background function is non-physical. For this reason and after determining the final value of the smoothing parameter, it is useful to over plot the background derivative and the resulting $\chi(k)$, and this is shown in Figure 23.
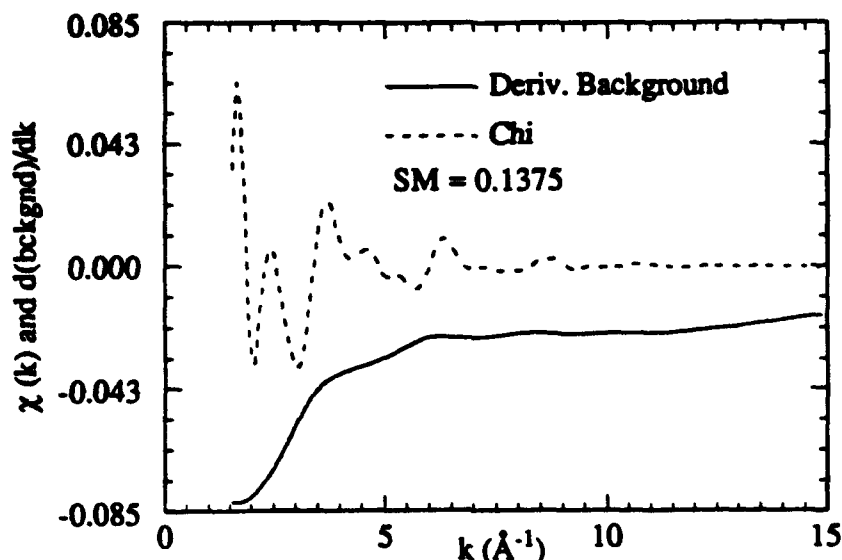


Figure 23: Background derivative and EXAFS function $\chi(k)$ vs photoelectron wave number k in $\mathring{A}^{-1}$ for 2,5 dibromothiophene monomer.

## 4.1.5 Normalization

After the background has been subtracted from the data, the next step is to normalize the EXAFS oscillations to enable meaningful comparisons and transferability of spectra taken on different samples. If model compounds are to be used as standards in the later detailed analysis, energy independent normalization may be used. The normalized EXAFS oscillations are then given by [32]

$$\chi(E) = \frac{\mu(E) - \mu_b(E)}{\mu(E_i)} \tag{7}$$

where $\mu(E)$ is the un-normalized data from which the post-edge background has been removed, $\mu_b(E)$ is the pre-edge background function determined in Section 4.1.2 and $E_i$ is a systematically chosen point such that it lies on a node of the background determined in Section 4.1.4. When

40

studying several samples of a given system, it is important that the same energy value be used to maintain consistency.

Once the data set has been normalized, it must be written in a form conducive to detailed Fourier analysis. This procedure writes only the normalized $\chi$ into a file that can be read by a program that analyzes and fits the $\chi$ data. A plot of the normalized $\chi$ for 2,5 dibromothiophene monomer is shown in Figure 24.
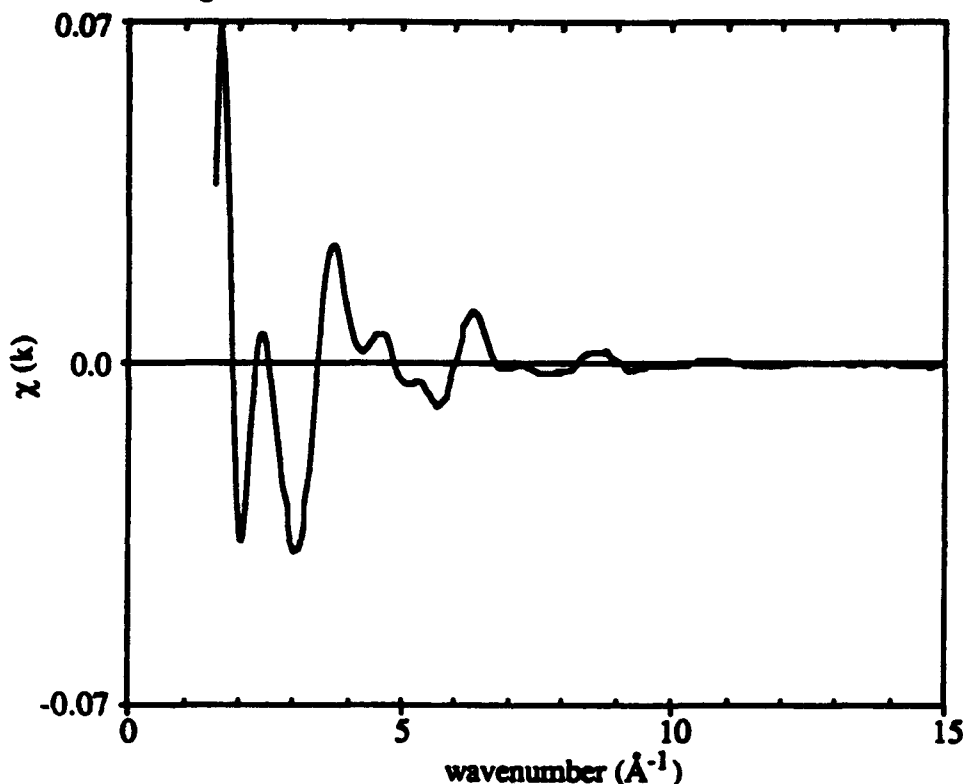
Figure 24:    Normalized EXAFS function $\chi(k)$ vs photoelectron wavenumber k in inverse Å for 2,5 dibromothiophene monomer.

## 4.2   Fourier Analysis and Curve Fitting

Once a careful preliminary analysis has been completed, detailed Fourier analysis and quantitative comparison may commence. It is well established [8,12,32] that the FT can be used to extract structural information from equation 1 since it is essentially a sum of sines and

41

exponentials. The reason that it is possible to isolate data corresponding to different radial distances is that the sine term contains the strongest k dependence.

There are several ways to extract information from equation 1, and the method(s) used for a given study will depend on what questions are being asked. Three well-known techniques are curve-fitting, curve calculation, and visual comparison. Often two or more of these methods are used together. The program used in this part of the analysis enables one to over plot several $\chi$ or FT($\chi$) spectra, fit data to a reference material or theoretical information, and calculate EXAFS spectra given a reference material or theoretical modeling information. Because the fine structure corresponding to different shells oscillates at different frequencies, spectrally isolating these contributions will greatly simplify the analysis. As a result, Fourier filtering and back transformation are available in the programs to isolate single shell data.

For a theoretical treatment one may use the calculated phase shifts and backscattering amplitudes of Teo and Lee [35] (plane wave approximation), McKale et al [36] (curved-wave effects, ground state potentials) or output from the program FEFF [16-18] (curved-wave, single scattering, includes electron self-energy). This is particularly useful when a suitable reference compound is difficult or impossible to obtain, although one must be particularly careful to properly normalize the data as a function of energy in this case. If a reference material is available for the fitting or calculation, it should be used instead of the theoretical values. This method is particularly useful when comparing the sample to a well-characterized standard. In addition to providing a reference for phase shifts and backscattering amplitudes, the use of model compounds allows the analyst to visually compare his experimental and calculated or fitted data to the model.

Two other features which are useful are plotting of $k^n\chi(k)$ vs. k and FT ($k^n\chi(k)$) vs. R, where $0 \leq n \leq 3$ is used as a weighting factor to highlight a particular portion of the spectrum, as described in Section 2.1. The k-weighting power should be chosen so as to give a constant amplitude of the weighted data over the range to be transformed. The choice of weighting will also give information on the relative Z contributing to various shells. Higher-Z materials will show a larger contribution in the $k^3$ transform than the $k^1$ transform, thus allowing identification of species

42

as a function of Z. Generally the k weighting given to a particular data range to produce uniform amplitude can be determined by limitations imposed on that data by the signal-to-noise ratio [32].

It is a common procedure to fit the data from one or more shells to an EXAFS parametrization function by numerical methods on a digital computer [32]. An examination of equation 1 indicates that $N$, $F(k)$, $\sigma$, $\lambda$, $R$, $E_0$, $\delta(k)$, $\Delta$, and $S_0^2$ must be input to the fitting routine. If model compounds are used, then $\lambda$, $\Delta$, and $S_0^2$ are obtained from the amplitude of $\chi(k)$ of the model and $F(k)$ and $\delta(k)$ are accounted for in the phase-corrected filtering of the shell(s) also from the model compound. The analyst may then vary up to four parameters per shell: $N$, $R$, $\Delta\sigma^2$, and $E_0$. Remember that the disorder calculated is the relative disorder between the model and the unknown and will, in general, include thermal as well as structural differences between the model compound and the unknown.

The data are fit using standard [37] nonlinear least squares fitting routines. The standard method for fitting the data is to minimize the sum of the squares of the weighted residuals, which is given by [32]

$$S^2 = \sum_i s_i^2 = \sum_i (\chi_i^F - \chi_i^E)^2 W_i \qquad (8)$$

and is relative to which parameters are being varied.

The sum in equation 8 is taken over the range of data being fitted, $\chi^F$ and $\chi^E$ are the fitted and experimental EXAFS functions, respectively, and $W$ is the reciprocal of the standard deviation. One should be cautioned that the result obtained may be a local rather than the absolute minimum. To check the consistency of the solution with the data, it is wise to over plot $\chi^F$ and $\chi^E$, and to run the fits with different, yet still reasonable, starting estimates.

# Section 5
# RESULTS

## 5.1 Spectroscopic Ellipsometry

It was found that spectroscopic ellipsometry was a viable technique for estimating film thickness for those samples which were deposited onto Si wafers. Due to the low reflectivity of Be foil, those samples were not suitable for this technique. However, Be proved to be a better substrate from an XAFS point of view, as sharp spikes probably due to diffraction from ordered structures in the Si wafers prevented collection of usable XAFS data from samples on Si.

## 5.2 Scanning Electron Microscopy

SEM was used to estimate the thickness of Sample 179. No photographs were available, but the film thickness was estimated to be 1 $\mu$m.

## 5.3 X-ray Absorption Fine Structure

During two trips to Brookhaven National Laboratory a total of 41 data scans were collected. Twenty-four hours of available beam time were used during both runs. Each of the samples was scanned twice with the parameters in Table 2 or 3 depending on the sample and edge, except where noted. For sulfur, Table 3 is modified to an analogous region about the sulfur K-edge. Table 4 lists sample name which will be referred to in the rest of the report, material, substrate, beamline, absorption edge, data collection mode (transmission-T or fluorescence-F), number of scans for each sample at each edge, and number of usable full scans.

**Table 4:** Listing of all XAFS scans for each of the samples by name, material description, substrate, beamline, absorption edge, mode of collection (T for transmission, F for fluorescence), total number of scans, and number of analyzable full scans. The names are translated as: Edge followed by type of monomer or sample number. For example, BR179 is the bromine K-edge data for sample # 179.

| Sample Name | Material | Substrate | Beamline | Edge | Mode (T/F) | number of scans | usable full scans |
|---|---|---|---|---|---|---|---|
| STH | Thiophene monomer | Filter Paper | X-19A | S | T | 5 | 1 |
| SCLTH | 2,5 dichloro- | Filter | X-19A | S | T | 3 edge | 0 |
| CLTH | thiophene | Paper | X-19A | Cl | T | 3 edge+2 | 2 |
| SBRTH | 2,5 dibromo- | Filter | X-19A | S | T | 6 edge +1 | 1 |
| BRTH | thiophene | paper | X-11A | Br | T,F | 2 edges +4 | 4 |
| BR175 | BRTH film | 0.015" Be foil | X-11A | Br | T,F | 1 edge +2 | 2 |
| S179 | BRTH | 0.001" | X-19A | S | T | 1 edge +2 | 2 |
| BR179 | film | Be foil | X-11A | Br | T,F | 1 edge +2 | 2 |
| BR180 | BRTH film | Si wafer | X-11A | Br | T,F | 1 | 0 |
| BR181 | BRTH film | Si wafer | X-11A | Br | T,F | 6 | 0 |
| S183 | Thiophene film | 0.0006" Be foil | X-19A | S | T | 4 edge + 1 | 1 |
| S185 | CLTH | 0.015" | X-19A | S | T | 1 edge + 2 | 2 |
| CL185 | film | Be foil | X-19A | Cl | T | 1 edge + 2 | 2 |

### 5.3.1 S and Cl XAFS Data

#### 5.3.1.1 Argon Results and Edge Jumps

Recall Beer's Law, $I = I_0 e^{-\mu x}$ , which governs the absorption process. Solving this equation for $\Delta\mu x$ and expressing it in terms of an edge jump gives

$$\Delta\mu x = \ln\left(\frac{I_0}{I}\right)_a - \ln\left(\frac{I_0}{I}\right)_b$$
$$= (\mu x)_a - (\mu x)_b$$

(9)

where $\ln(I_0/I)_a$ is the transmission data above the edge, $\ln(I_0/I)_b$ is the transmission data below the edge, and $\Delta\mu$ is the change in the absorption coefficient through the edge. The data collected are $\mu x$, so the comparisons will be those of Argon edge jumps. Assuming $\Delta\mu$ to be constant, the differences in argon edge heights can be related directly to differences in argon "effective thickness." Table 5 shows $(\mu x)_a$, $(\mu x)_b$ and $\Delta\mu x$ at the argon edge for each of the Cl and S (if available) data scans.

Table 5: Argon edge jumps for thiophene and Cl-containing thiophene samples collected in transmission. Sample names are those defined in Table 4 and column headings are defined in the text.

| Sample | $(\mu x)_a$ | $(\mu x)_b$ | $\Delta\mu x$ |
|--------|------------|------------|---------------|
| S185   | 0.19149    | 0.12477    | 0.06672       |
| CL185  | 1.73575    | 1.64085    | 0.09490       |
| SBRTH  | 0.20917    | 0.11225    | 0.09692       |
| CLTH   | 1.54413    | 1.47497    | 0.06916       |
| STH    | 0.41058    | 0.33808    | 0.07250       |

Argon absorption is a problem at low energies because of argon content in the air, argon impurities in standard He tanks, and the proximity of the argon K-edge to those of Cl (382 eV) and S (733 eV). Optimization of the sample will reduce the severity of truncation errors limiting the data range. Another solution to the argon problem is to enclose the samples in a vacuum chamber

47

rather than a helium-flushed chamber. Such a chamber could be constructed with window materials possessing the properties of good strength and transmission in the 2-4 keV range, such as Be foil, synthetic diamond or diamond-like carbon films. The advantage of a hard carbon window over Be is that Be is considered hazardous. Another possibility is argon entrapment in the films from the plasma deposition process. The present XAFS setup could not distinguish the source of the argon signal. The vacuum sample chamber would solve that problem, and also RBS could be used to determine argon content by a depth profile analysis. RBS has been done on earlier films [4] and no argon was detected from the plasma. Likewise, the S, Br and Cl K-edge jumps are listed in Tables 6 and 7. The data of Tables 6 and 7 can be illustrated by Figure 3 for an arbitrary edge of typical features.

Table 6: Energies and absorption values for edge features defined in Figure 3. The sample names were defined in Table 4. The pre-edge value $\mu x_{pre}$ was chosen as close as possible to -10 eV for consistency and the data have had the pre-edge function subtracted prior to tabulation. In the case of Br edges, the value given for "white line" is not the absolute maximum but the first local maximum above the edge because the shape of the Br edge is different than those of Cl and S.

| Sample | $E_{pre}$ (eV) | $\mu x_{pre}$ | $E_0$ (eV) | $\mu x_0$ | $E_{WL}$ (eV) | $\mu x_{WL}$ | $E_D$ (eV) | $\mu x_D$ | $E_P$ (eV) | $\mu x_P$ |
|---|---|---|---|---|---|---|---|---|---|---|
| BR175 | -9.71 | 0.00091 | 0.29 | 0.00572 | 5.44 | 0.02099 | 7.43 | 0.02049 | 11.49 | 0.02347 |
| S179 | -10.31 | -0.00179 | -0.30 | 0.13612 | 0.70 | 0.33541 | 4.70 | 0.12325 | 8.70 | 0.14877 |
| BR179 | -9.71 | 0.00304 | 0.29 | 0.02254 | 4.35 | 0.04905 | 6.34 | 0.04705 | 10.40 | 0.05540 |
| S183 | -9.51 | -0.00655 | 0.50 | 0.03512 | 1.50 | 0.05081 | 5.50 | 0.01633 | 10.49 | 0.02058 |
| S185 | -9.58 | -0.00022 | 0.43 | 0.14181 | 2.43 | 1.04057 | 6.43 | 0.42405 | 10.43 | 0.50008 |
| CL185 | -9.91 | -0.04363 | 0.09 | 0.58762 | 1.09 | 1.15056 | 3.10 | 0.38071 | 8.10 | 0.66359 |
| SBRTH | -9.58 | -0.00680 | 0.43 | 0.00110 | 2.43 | 0.31416 | 4.43 | 0.04068 | 8.43 | 0.09339 |
| BRTH | -9.71 | 0.01995 | 0.29 | 0.32860 | 4.35 | 0.9615 | 6.34 | 0.93445 | 10.40 | 1.10029 |
| CLTH | -9.80 | 0.00558 | 0.20 | 0.68306 | 1.19 | 1.02980 | 3.19 | 0.31580 | 5.19 | 0.65279 |
| STH | -10.31 | -0.00636 | -0.30 | 0.01576 | 0.70 | 0.15674 | 2.70 | 0.05393 | 4.70 | 0.06074 |
| BR181 | -9.71 | 0.00076 | 0.29 | 0.00920 | 4.35 | 0.01859 | 6.34 | 0.01805 | 11.49 | 0.02180 |

**Table 7:** Edge jumps referenced to the white line and the peak in each of the samples as described in Table 6.

| Sample | $\mu x_{WL}-\mu x_{pre}$ | $\mu x_p-\mu x_{pre}$ |
|---|---|---|
| BR175 | 0.02008 | 0.02256 |
| S179 | 0.33720 | 0.15056 |
| BR179 | 0.04601 | 0.05236 |
| S183 | 0.05736 | 0.02713 |
| S185 | 1.04080 | 0.50030 |
| CL185 | 1.19420 | 0.70722 |
| SBRTH | 0.32096 | 0.10019 |
| BRTH | 0.94155 | 1.08030 |
| CLTH | 1.02420 | 0.64721 |
| STH | 0.16310 | 0.06710 |
| BR181 | 0.01783 | 0.02104 |

### 5.3.1.2 XANES Results

Figures 25 - 31, inclusive, show the raw $\mu x$ spectra (a) and pre-edge subtracted un-normalized X-ray absorption near edge structure (XANES) spectra (b) for each of the samples at the S and, as appropriate, Cl edges. The general features described in the captions of Figure 3 and Tables 6 and 7 are apparent in the edge spectra and are presented in the following order: SBRTH (20), STH (21), CLTH (22), S179 (23), S183 (24), S185 (25), and CL185 (26). The sample names were defined in Table 4.
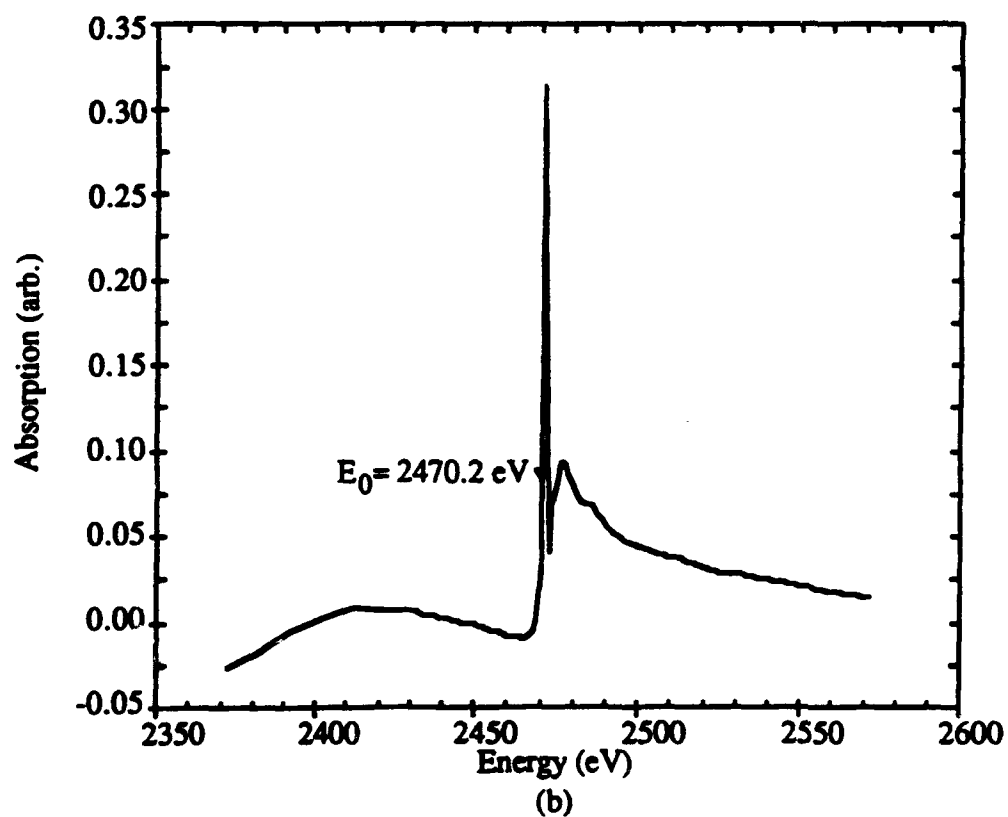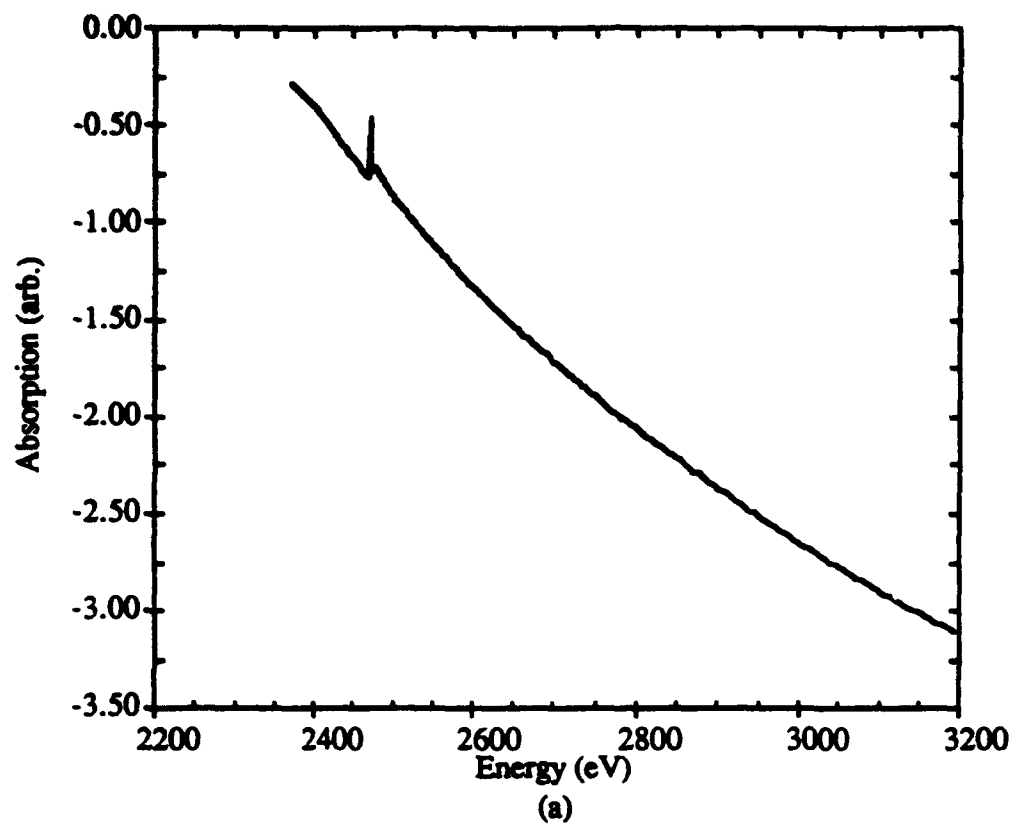
**Figure 25:** Raw μx spectrum (a) and S K-edge XANES (b) for 2,5 dibromothiophene in transmission

50
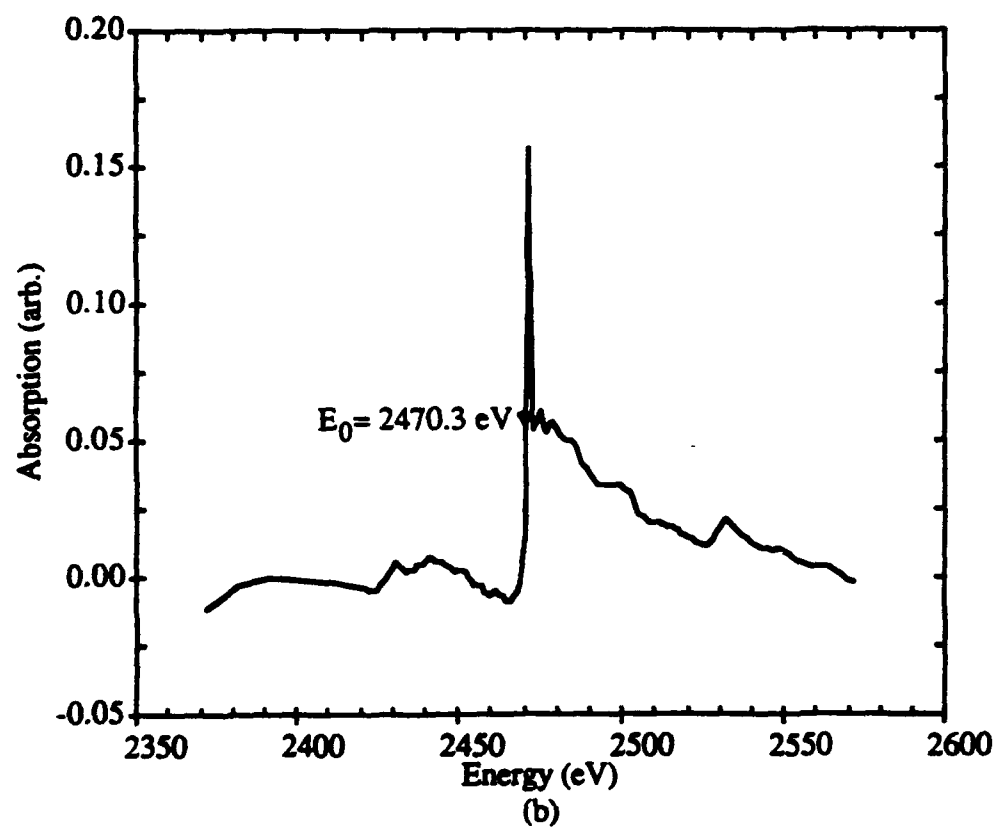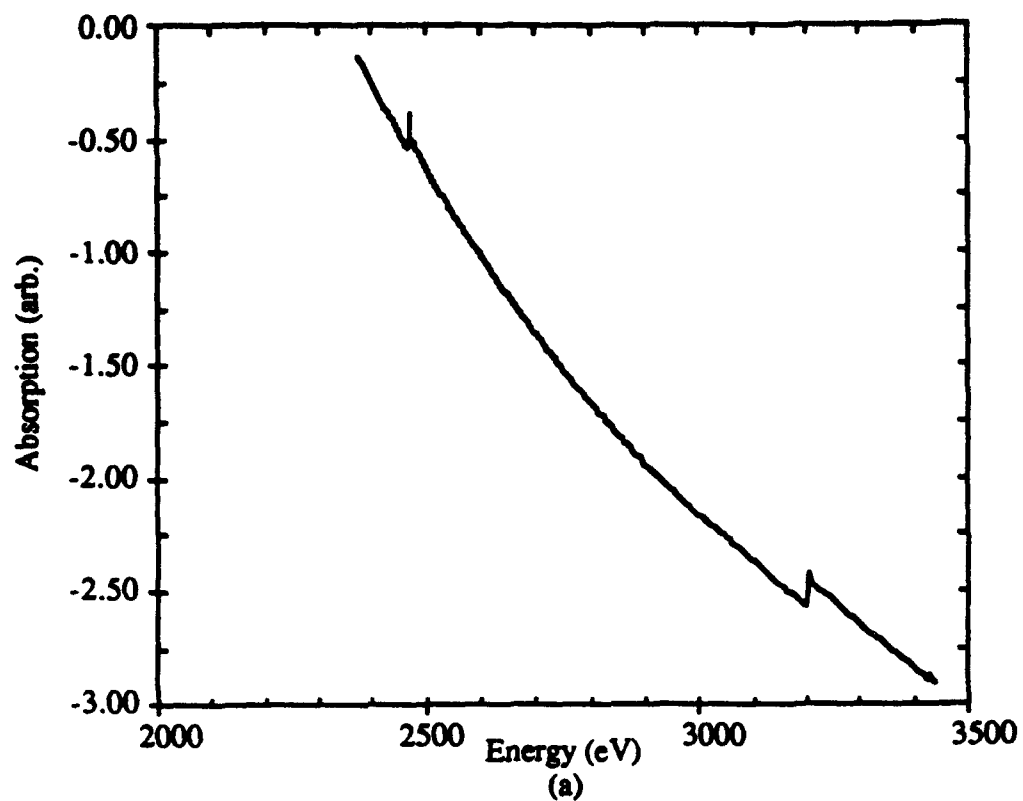
Figure 26: Raw μx spectrum (a) and S K-edge XANES (b) for thiophene monomer in transmission.
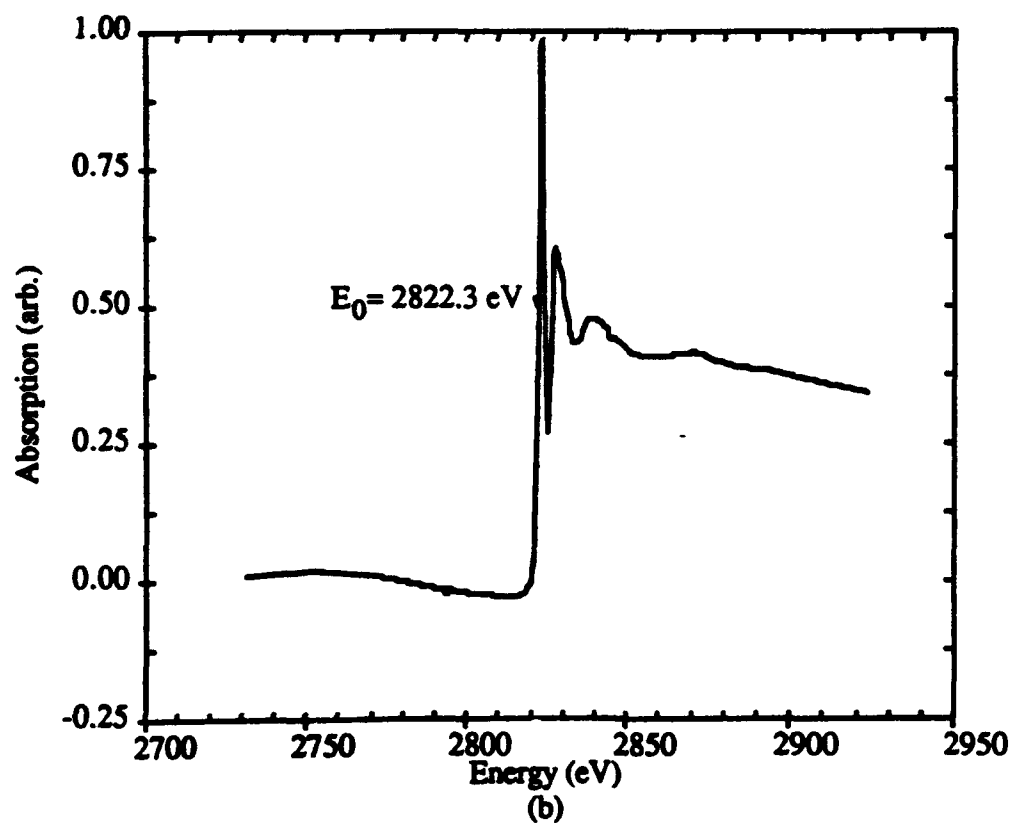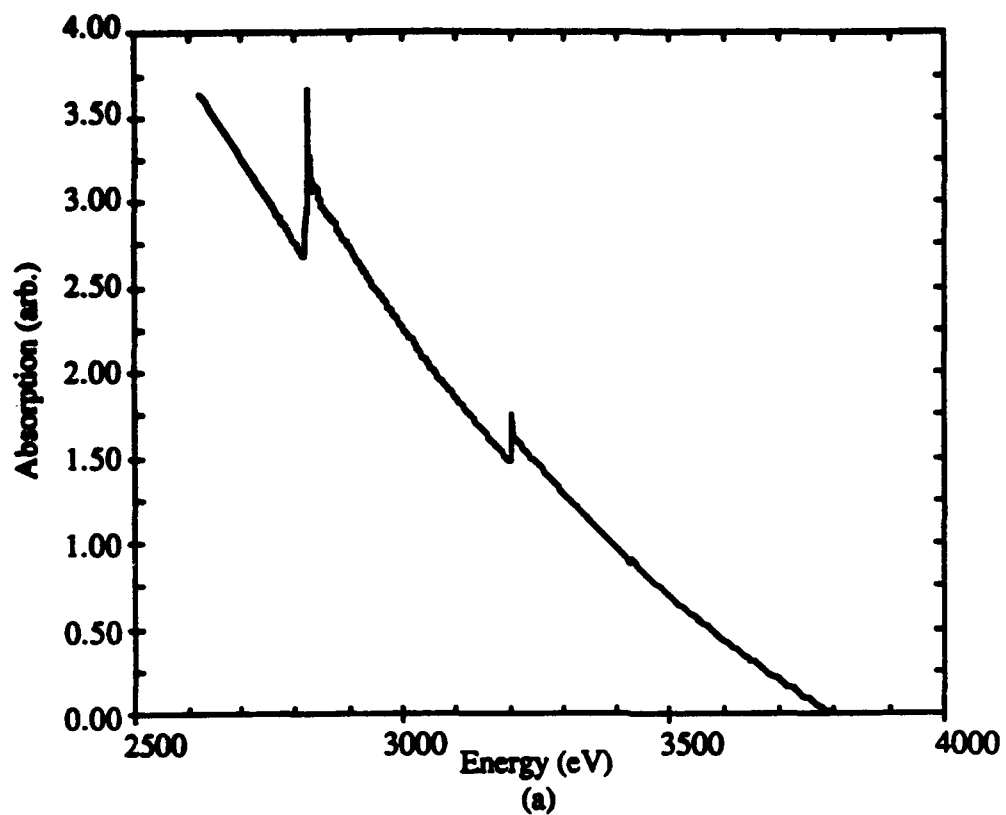
Figure 27:    Raw μx spectrum (a) and Cl K-edge XANES (b) for 2,5 dichlorothiophene
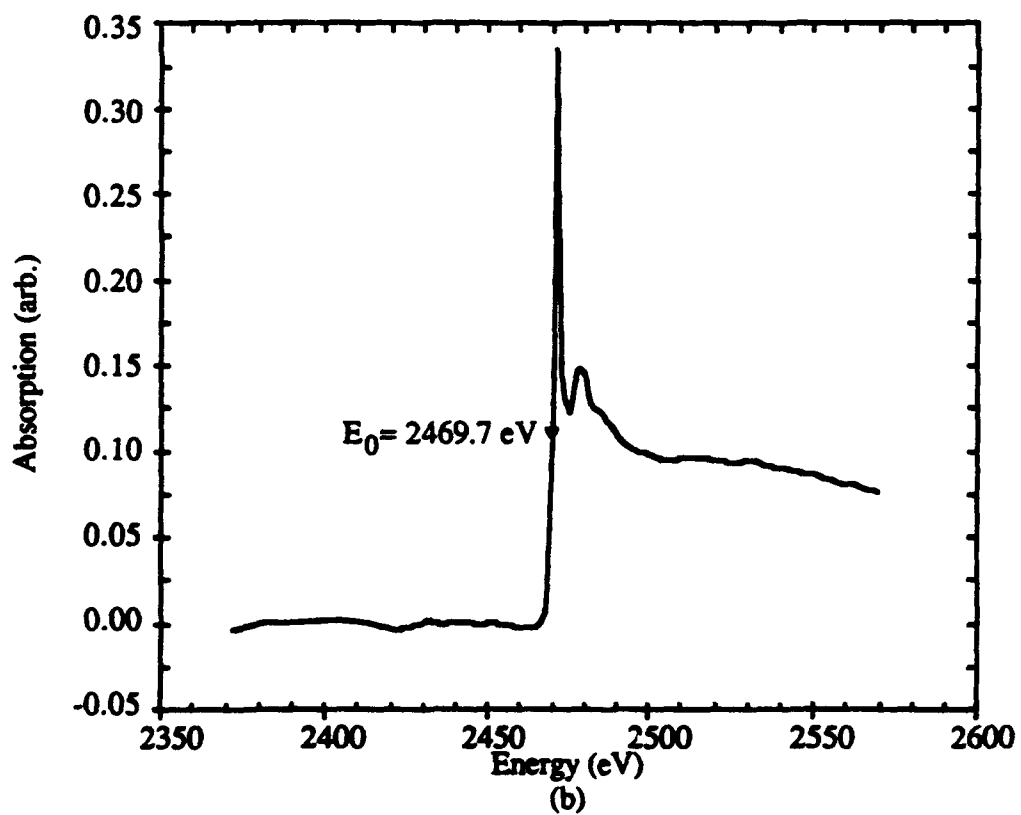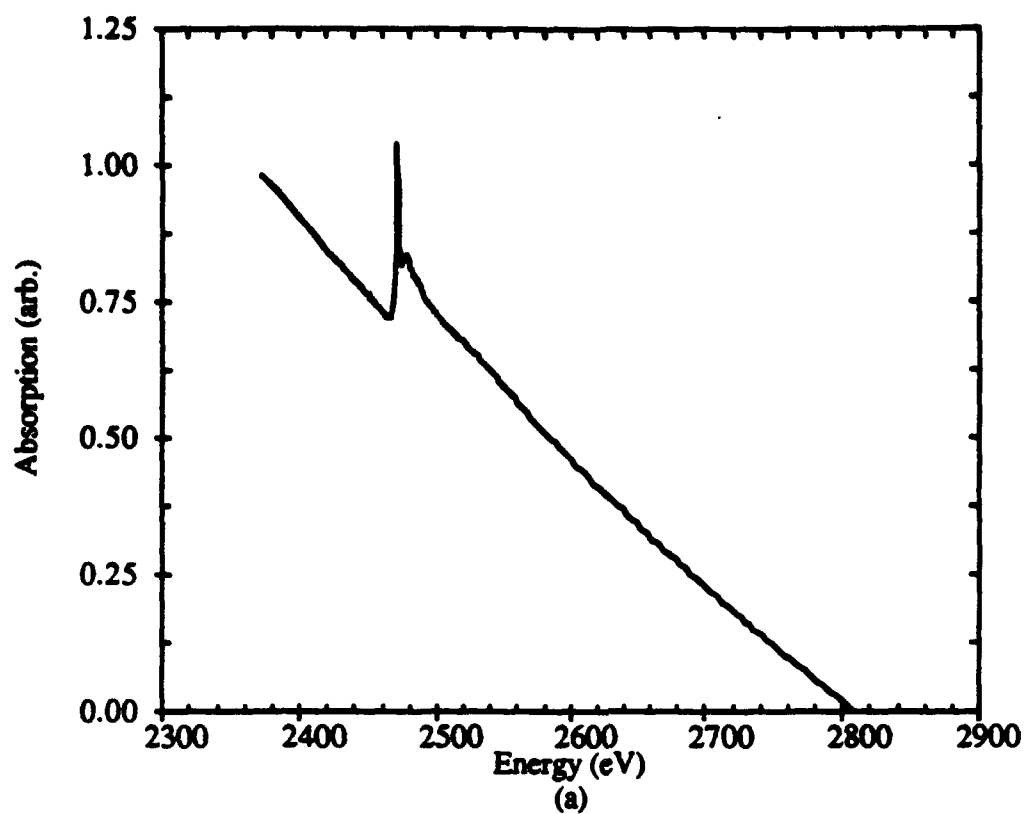monomer in transmission.

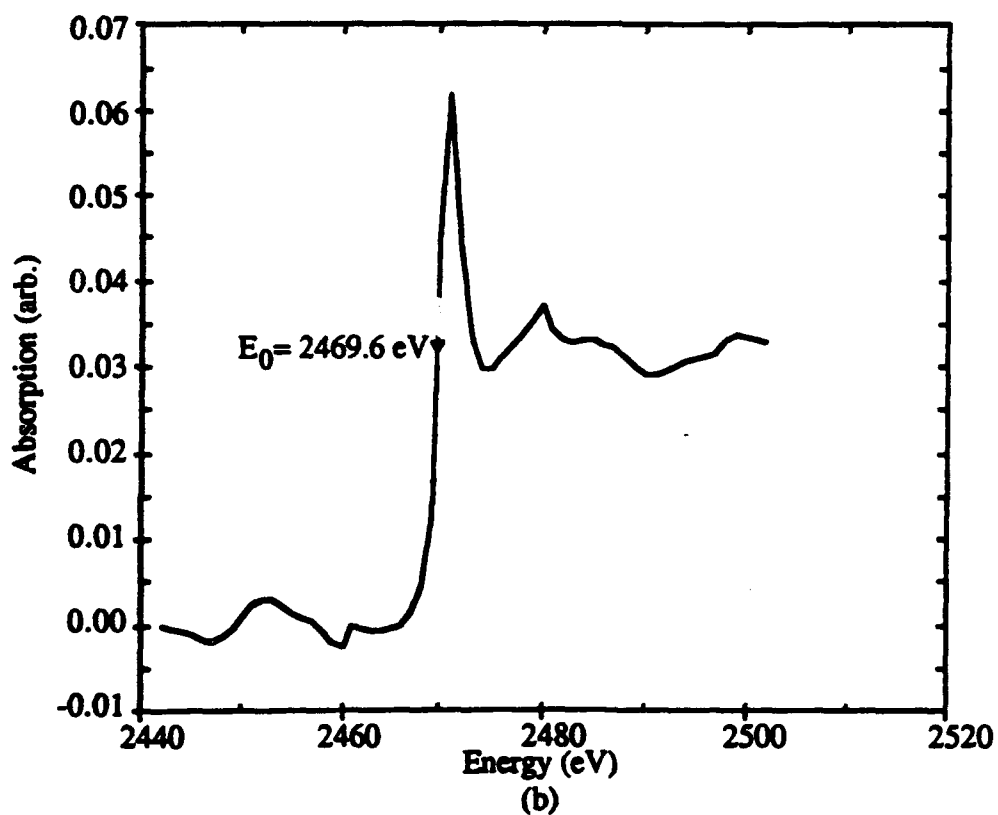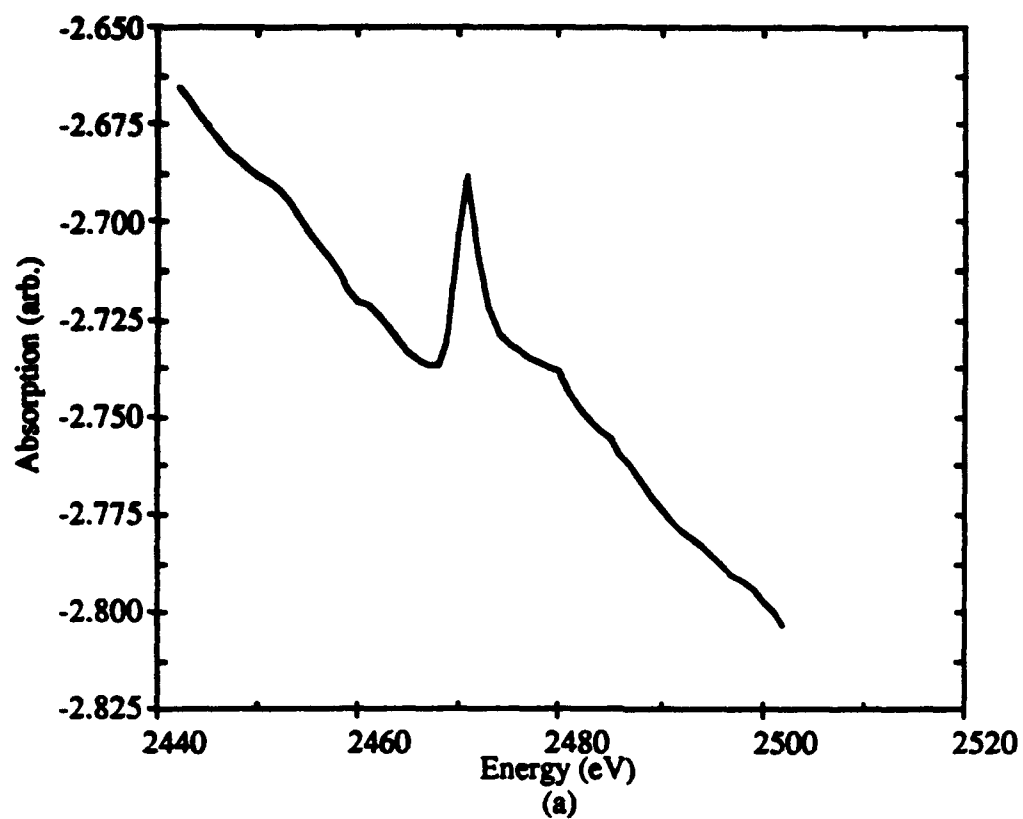Figure 28: Raw μx spectrum (a) and S K-edge XANES (b) for sample 179 in transmission.

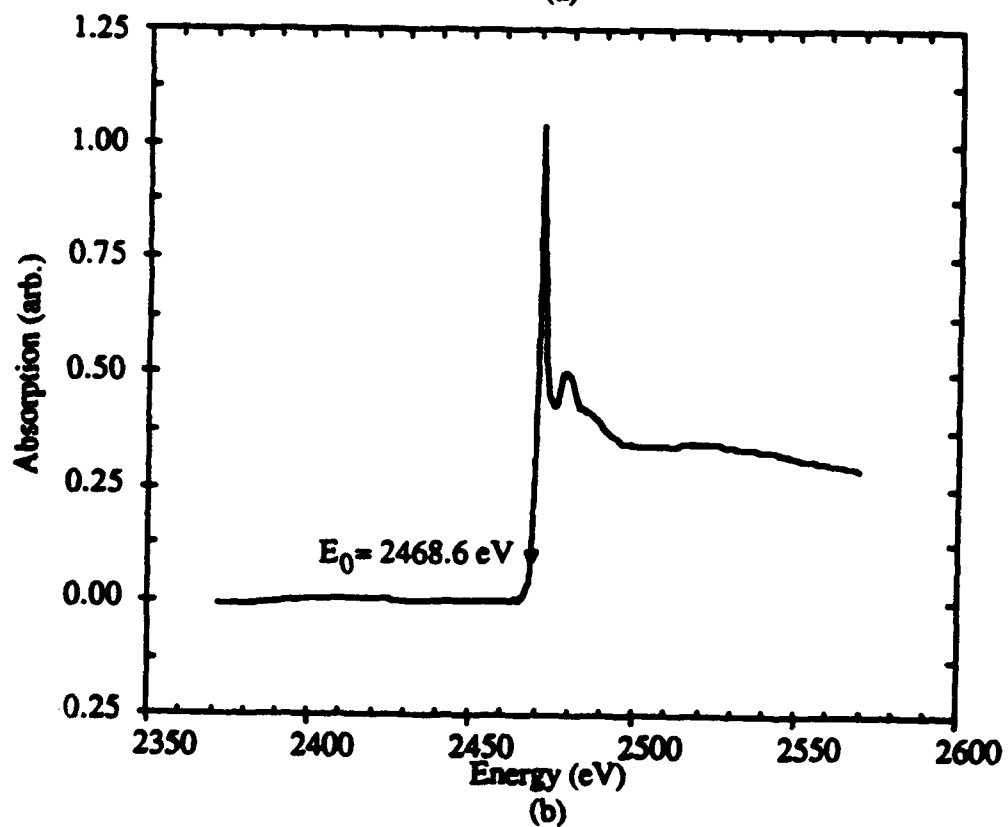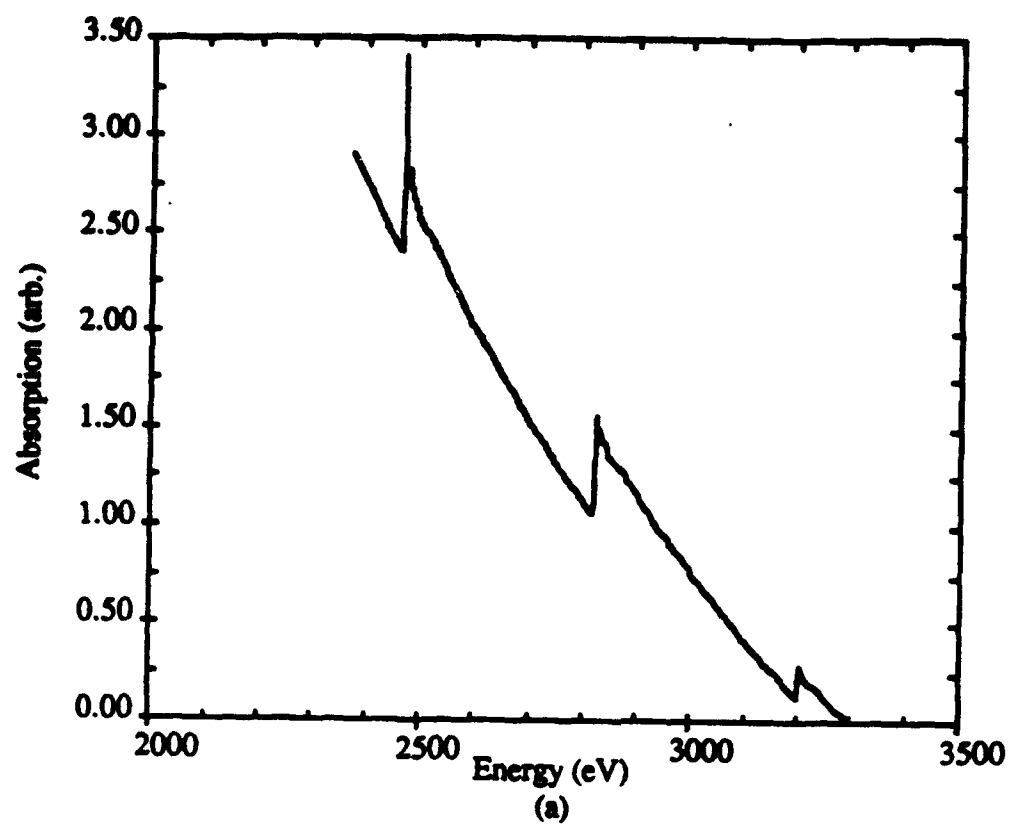Figure 29:     Raw μx spectrum (a) and S K-edge XANES (b) for sample 183 in transmission.

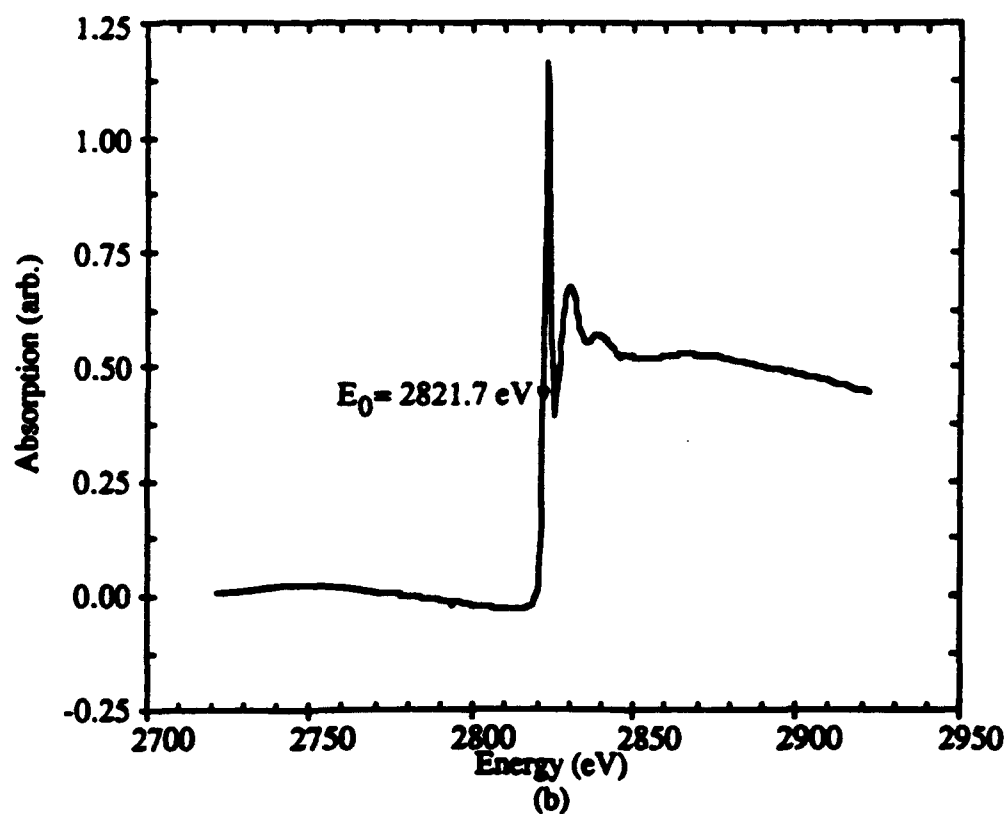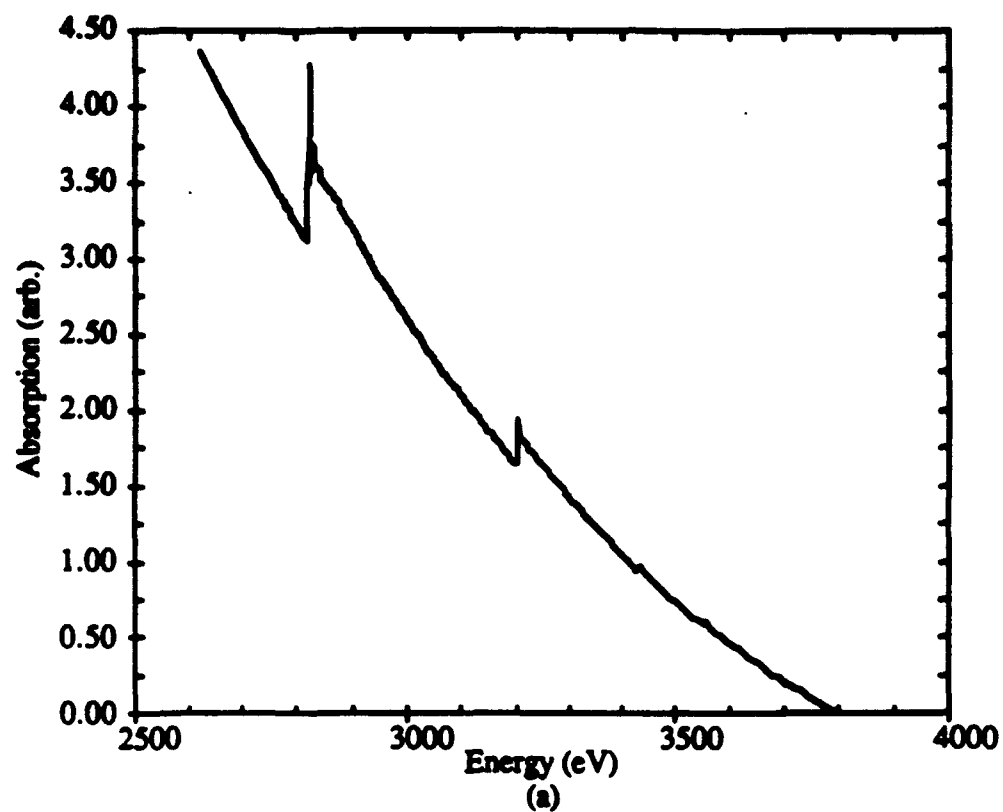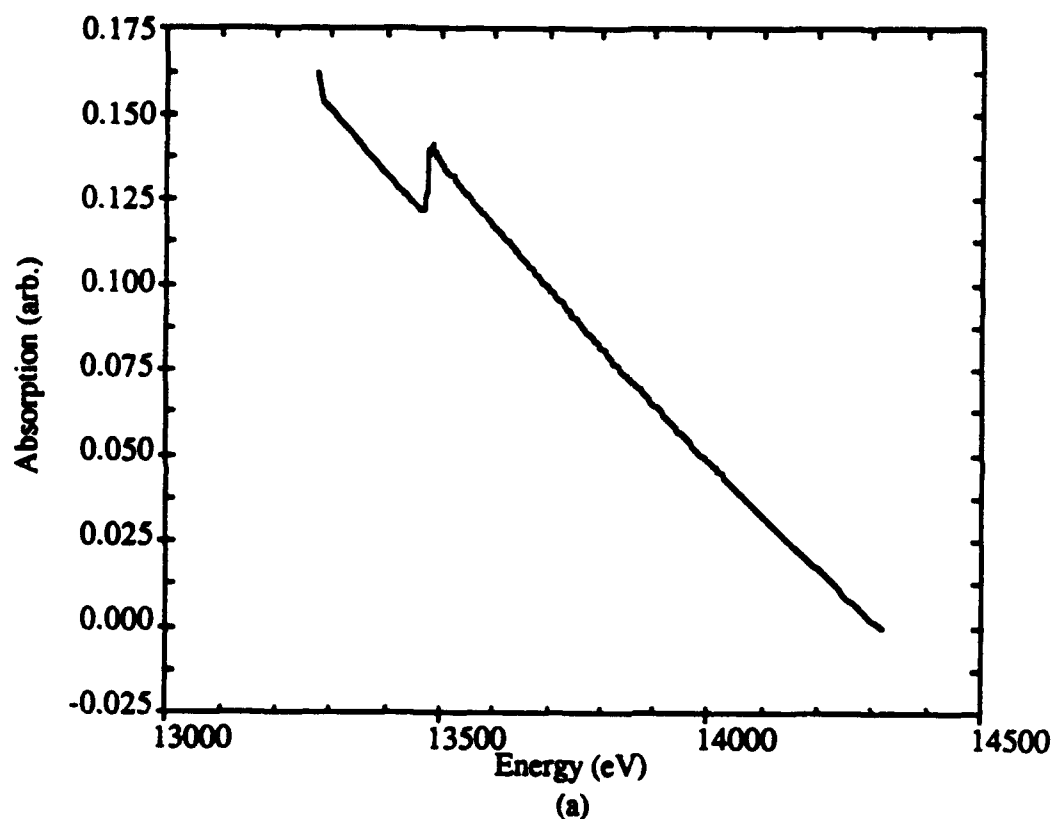Figure 30:    Raw μx spectrum (a) and S K-edge XANES (b) for sample 185 in transmission.

55

Figure 31:    Raw μx spectrum (a) and Cl K-edge XANES (b) for sample 185 in transmission.

## 5.3.2 Br K-Edge Data

The Br K-edge data in general contained more structure, as seen in Figures 11 and 13 especially, which is characteristic of heavier atoms. Those data are first presented graphically in a fashion similar to Figures 25 - 31 in Figures 32 - 34 for samples 175, 179, and 181, respectively, then discussion of curve-fitting will take place followed by results of using the 2,5 dibromothiophene monomer as a Br-S standard.
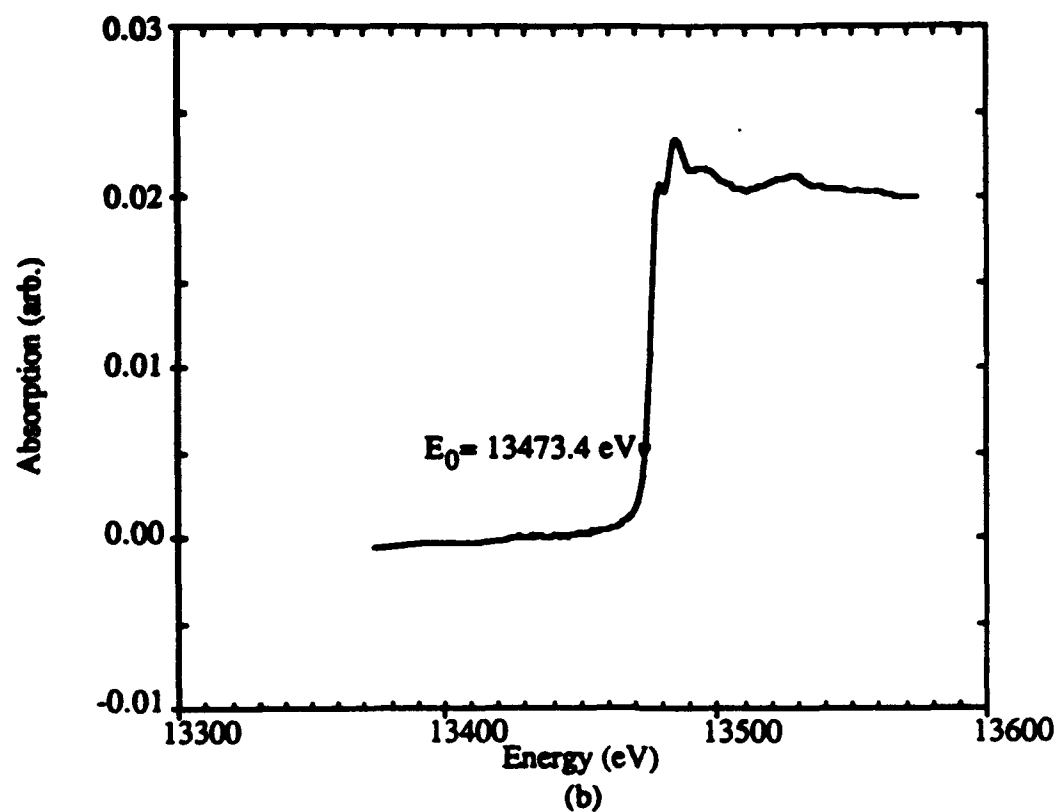


(a)

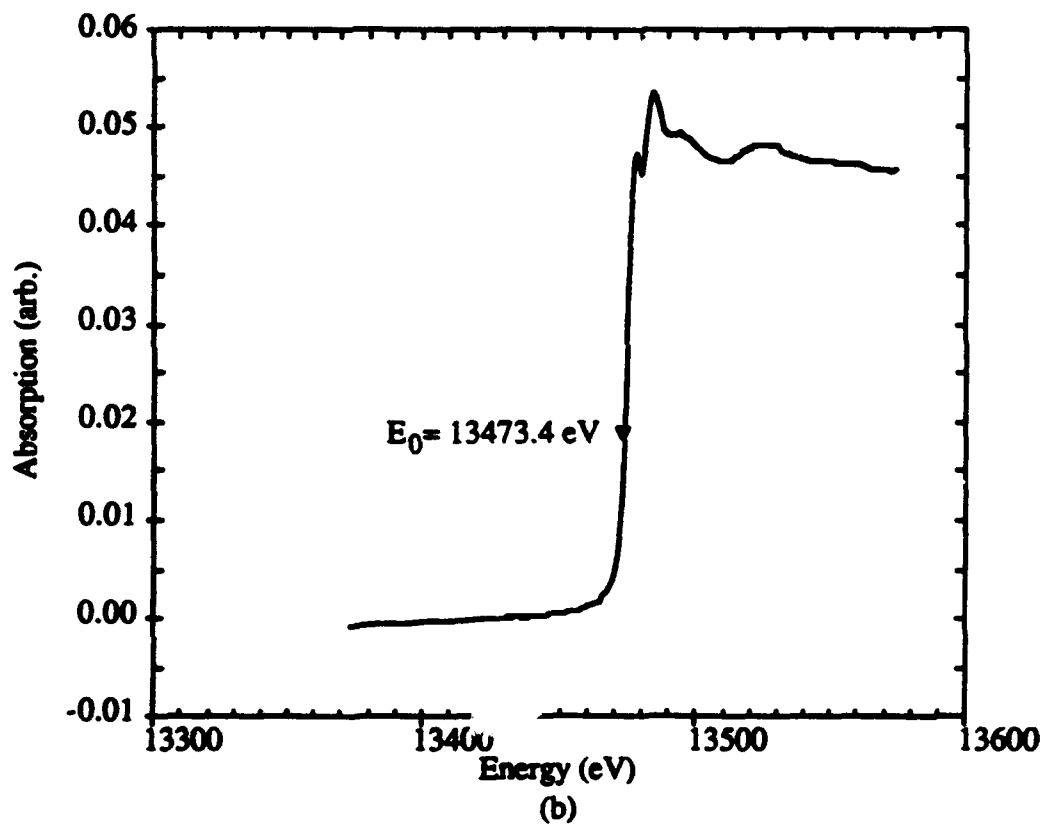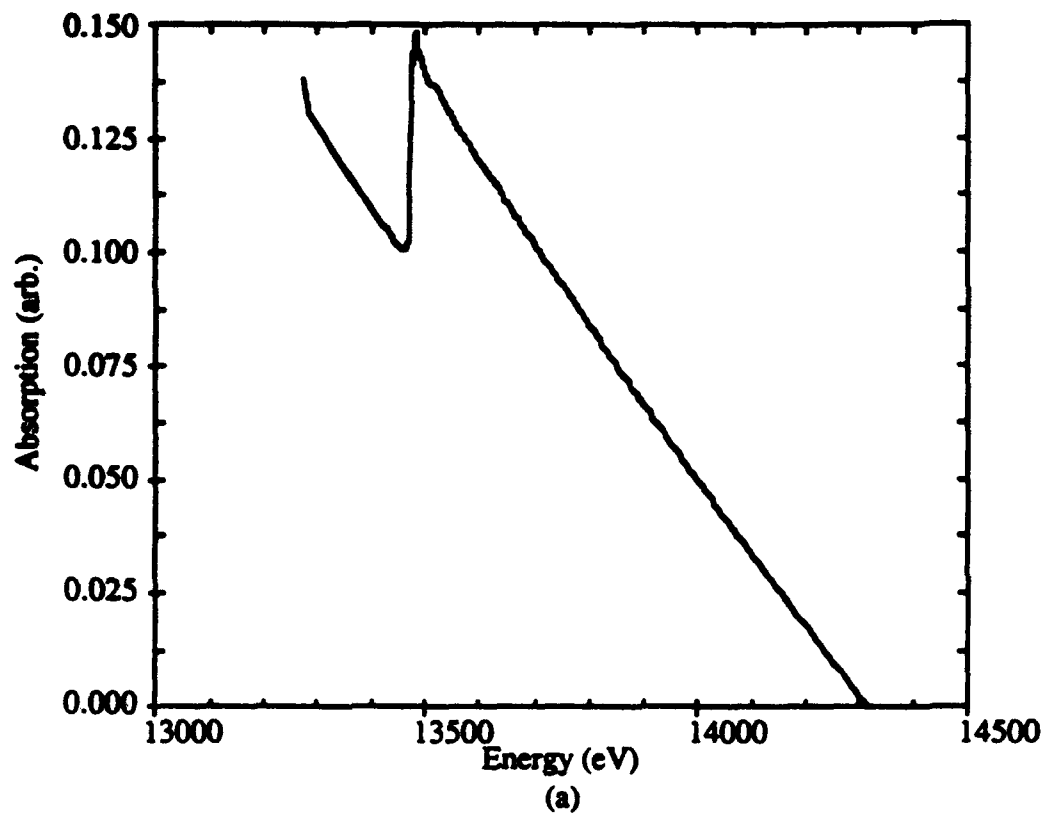Figure 32:    Raw μx spectrum (a) and Br K-edge XANES (b) for sample 175 in transmission.

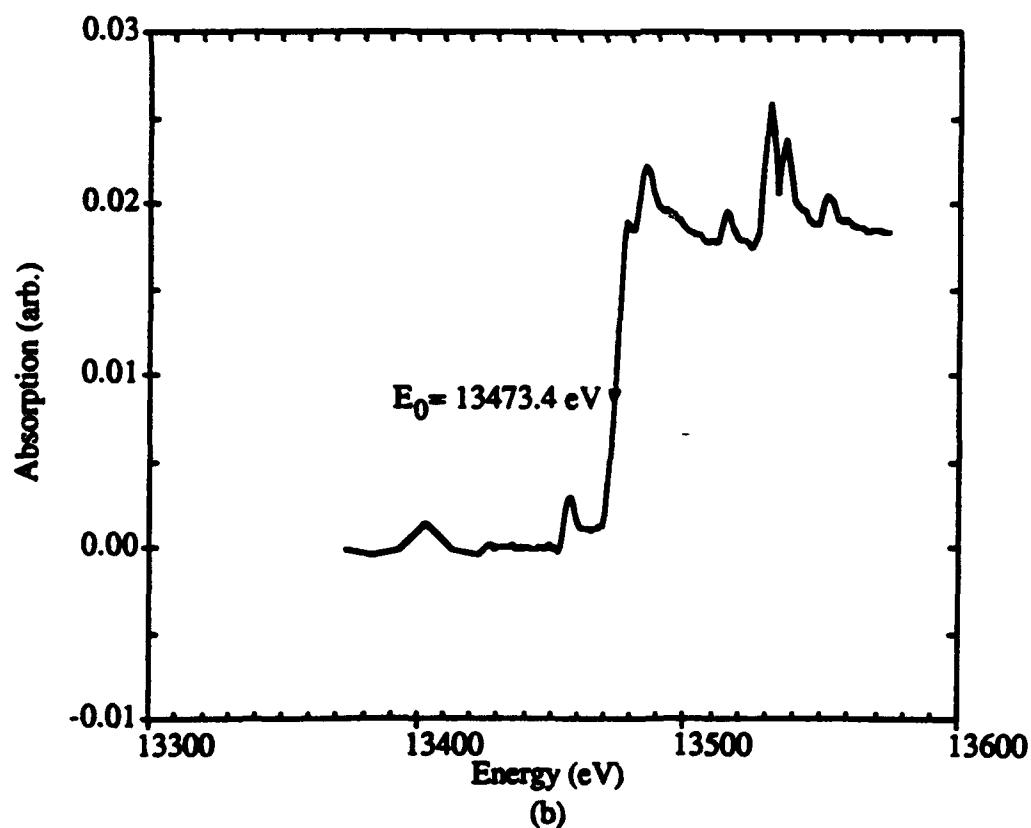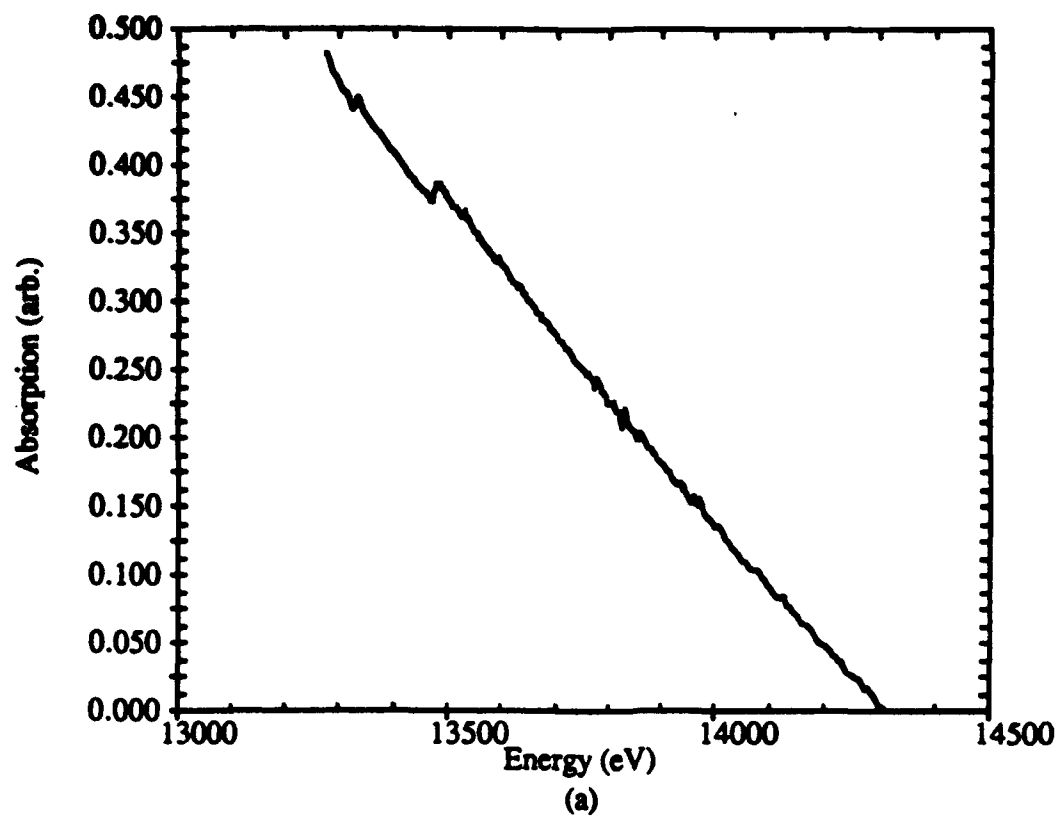Figure 33: Raw μx spectrum (a) and Br K-edge XANES (b) for sample 179 in transmission.

59

Figure 34:  Raw µx spectrum (a) and Br K-edge XANES (b) for sample 181 in transmission. Note the sharp features in the spectrum due to diffraction by the substrate.

A look at Figures 32-34 immediately indicates that the data from sample 179 holds the most promise for extracting meaningful results at this stage of the project, and those data will be used in the fitting procedure which follows, with the 2,5-dibromothiophene monomer data forming an empirical standard.

Figure 35 shows the result of shifting the FEFF calculation by $\Delta V_0 = -5eV$ and comparing the experimental $\chi(k)$ from 2,5 dibromothiophene monomer with the theoretical calculation. It can be concluded from that plot that within the theoretical and experimental constraints the monomer data can be used as an empirical standard for curve-fitting of $\chi(k)$ for the BRTH films since the theoretical and experimental curves only significantly differ by a constant shift in k-space. The experimental data are better because they are less sensitive to normalization errors and the theory does not predict the amplitude correctly [16-18].
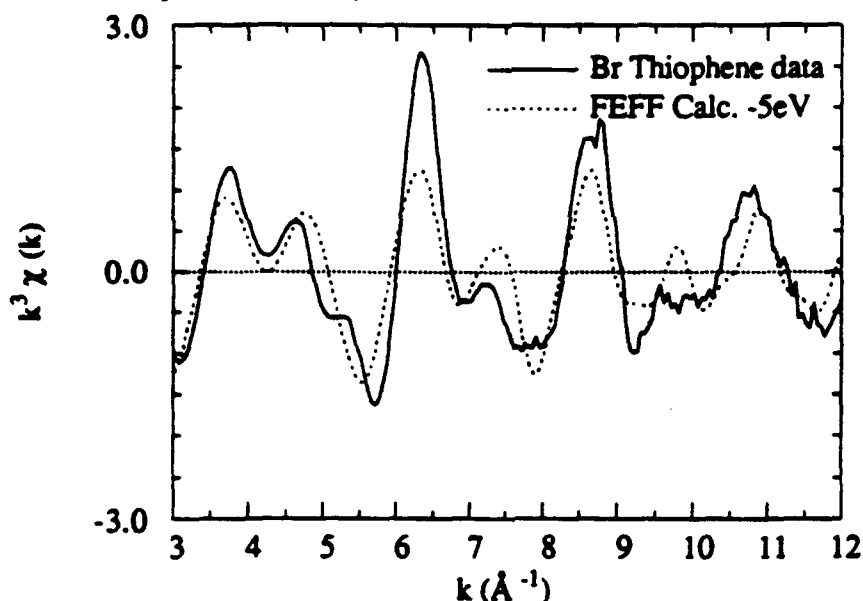


Figure 35: Overplot of BRTH monomer data and the FEFF-calculated $k^3 \chi(k)$ functions vs wavenumber in $Å^{-1}$ with a $V_0$ shift of -5eV applied to the FEFF calculation.

In Figure 36 $|FT (k^3\chi(k))|$ has been plotted for the monomer and sample 179. The FT's were made over the range 1.86-12.52 and 1.91-12.17 $Å^{-1}$, respectively. The first four peaks in the monomer are followed quite closely by the thin film, but the additional features in the thin film spectrum are quite interesting also.

61
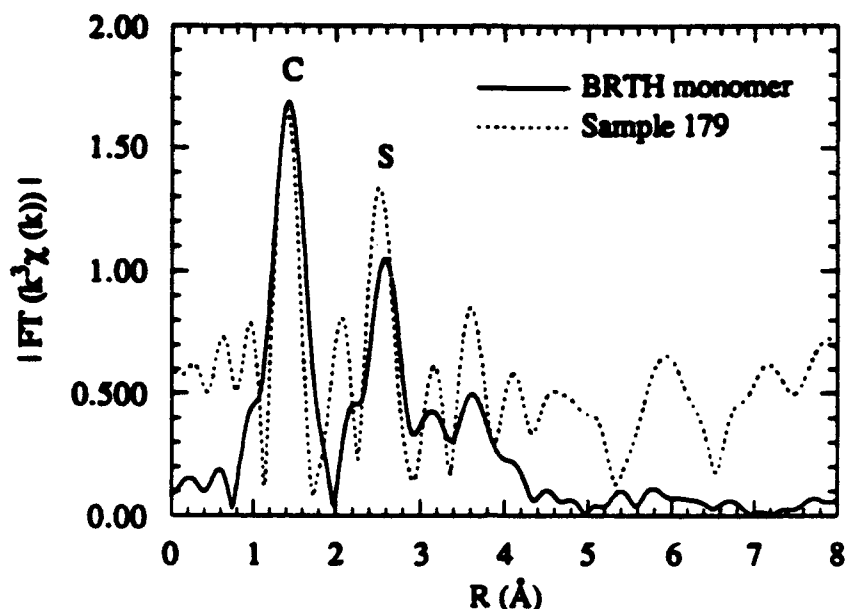
Figure 36: IFT $(k^3\chi (k))$I vs radial distance in Å for 2,5 dibromothiophene monomer and Sample 179 for Br K-edge EXAFS.

In order to prepare the sample 179 data for curve-fitting, inverse FFT filtering was done to isolate the $\chi$ contribution from each shell or multiple shells, according to Eq. (1). The inverse FFT window was determined by analyzing the extent of the peaks in the IFTI and back transforming over that range. Phase reference files were made using the monomer data by the same procedure. The inverse FT R-ranges are given in Table 8.

**Table 8:**  Inverse FFT and reference file parameters for $\chi(k)$-fitting of Sample 179 $\chi(k)$ data.

| Sample | Shell | R-left (Å) | R-right (Å) | R-ref. (Å) |
|---|---|---|---|---|
| BRTH monomer | 1 C | 0.74 | 1.98 | 1.85 |
| | 1 S | 1.98 | 2.94 | 3.085 |
| Sample 179 | 1 C | 1.14 | 1.72 | |
| | 1 S | 2.26 | 2.92 | |
| | 1 C + 1 S | 1.14 | 2.92 | |

Figures 37, 38 and 39 show the results of fitting the sample 179 data using the nonlinear least-squares fit algorithm described in Section 4 with the monomer reference files as described in Table 8. The results of those fits are given in Table 9. The fits were all done over the range 2-11 $\text{Å}^{-1}$. The $\Delta\sigma_i^2$ values are negative as should be expected since $\Delta\sigma_i^2$ is the disorder relative to the *liquid* monomer, i.e., the solid film is less disordered.



Figure 37: Overplot of data, fitted curve and residuals for 1 shell consisting of 1 C at 1.85Å in the model with 4 floating parameters for sample 179.
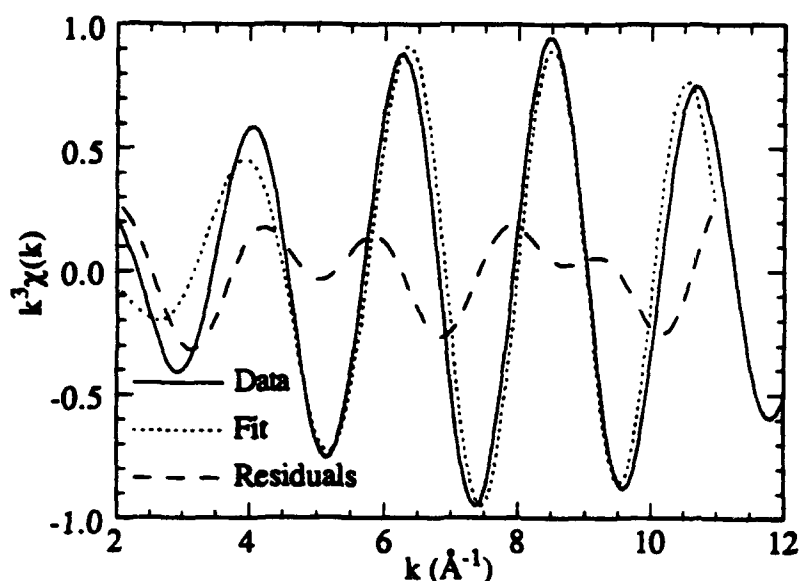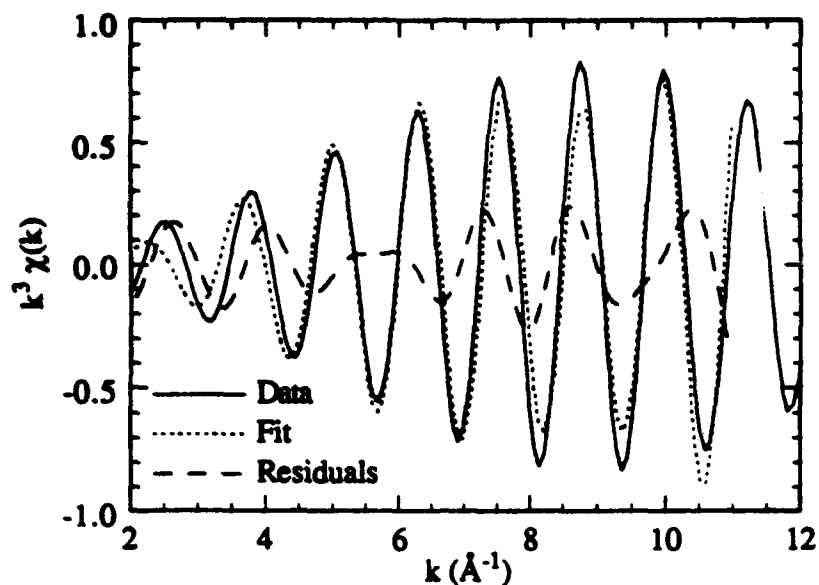
Figure 38: Overplot of data, fitted curve, and residuals for 1 shell consisting of 1 S at 3.09 Å in the model with 4 floating parameters for sample 179.
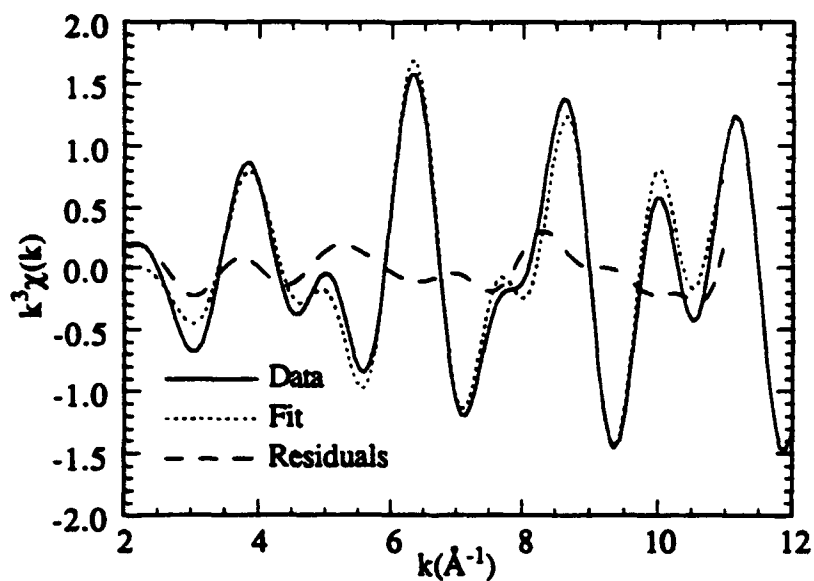


Figure 39: Overplot of data,fitted curve and residuals for 2 shells consisting of 1 C at 1.85 Å and 1 S at 3.09 Å in the model with 8 floating parameters for sample 179.

# SECTION 6

## CONCLUSIONS

In this study, we've shown the feasibility of developing X-ray Absorption Fine Structure spectroscopy as a useful technique for investigating structures of materials with potential laser-hardening applications. The near-atomic coordination information that the XAFS data provide could then be input to the deposition control system to improve processing of the film in order to tailor films of the appropriate thickness and / or growth rate for detailed analysis and investigation. The low values determined for the coordination numbers in Table 9 indicate that the thickness of the film was probably too low for proper transmission. This thickness effect is well known in the XAFS literature, and for a detailed study a series of different thickness films is proposed to determine the optimum thickness. The thickness problem was especially noticeable for the S and Cl edges from the magnitude of the edge jumps.

The results of the bromine K-edge fits indicate that once the experimental setup is optimized for sulfur, data of resolution similar to that from the bromine edge should be obtainable with respect to the sulfur atoms, i.e., since the local thiophene structure is preserved (as concluded from the fit results on the Br edge data) cis- or trans- character of the films, within the limits discussed below, should be inferable from the sulfur data.

We also observed the problems associated with ordered substrates when using Si wafers for the Br-containing film samples. The presence of Bragg diffraction peaks in the $\mu x$ data from sample 181 corroborated that claim.

The next step in the analysis will involve a parametric sensitivity approach to the EXAFS data processing. In order to quantify the level of cis- or trans- conformation in the plasma polymerized films, physical constraints on the molecular geometry must be inferred from the amount of noise in the data. The Matlab matrix laboratory programming system will be implemented on a Sun workstation to analyze the noise level by quantitatively analyzing how sensitive the fit results are to finite alterations of the raw data, which will remove some of the arbitrariness associated with current analysis techniques. A consistent, reproducible methodology

67

will be developed to determine the pre-edge, edge, and background by applying strictly objective criteria to the data. Over the course of development, the new package will be tested at each stage of development using well-characterized samples. Initially metal foil data will be used for this purpose, and as the algorithm becomes more refined, well-characterized oligothiophenes are hoped to be employed for this purpose to show applicability to polymer systems, and beam time at the NSLS has been applied for to make the necessary XAFS measurements.

# References

1. D. S. Chemla and J. Zyss, Eds., *Nonlinear Optical Properties of Organic Molecules and Crystals*, vol. I & II (Academic Press, NY, 1987).

2. A. F. Garito, C. C. Teng, K. Y. Wong, and O. Zammani'Khamiri, *Mol. Cryst. Liq. Cryst*. **106**, 219 (1984).

3. R. A. Hahn and D. A. Bloor, Eds., *Organic Materials for Nonlinear Optics II* (Royal Society of Chemistry, Wiltshire, 1991).

4. P. Haaland and J. Targove, *Appl. Phys. Lett*. **61**, 34 (1992).

5. P. N. Prasad and D. J. Williams, Eds., *Introduction to Nonlinear Optical Effects in Molecules and Polymers* (Wiley, NY, 1990).

6. D. R. Mullins, (American Vacuum Society, Chicago, IL, 1992).

7. L. C. Feldman and J. W. Mayer, *Fundamentals of Surface Science and Thin Film Analysis* (North-Holland, New York, 1986), p. 196.

8. D. E. Sayers, E. A. Stern, and F. W. Lytle, Phys. Rev. Lett., **27**, 1204 (1971).

9. E. A. Stern in *X-ray Absorption: Principles, Applications, Techniques of EXAFS, SEXAFS, and XANES*, D.C. Koningsberger and R. Prins, eds. (John Wiley, New York, 1988), pp. 3-53.

10. C. A. Ashley and S. Doniach, Phys. Rev. B, **11**, 1279 (1975).

11. D. C. Koningsberger, in *X-ray Absorption: Principles, Applications, Techniques of EXAFS, SEXAFS, and XANES*, D. C. Koningsberger and R. Prins, eds. (John Wiley, New York, 1988), pp. 163-210.

12. E. A. Stern, D. E. Sayers, and F. W. Lytle, Phys. Rev. B, **11**, 4836 (1975).

13. S. M. Heald, in *X-ray Absorption: Principles, Applications, Techniques of EXAFS, SEXAFS, and XANES*, D. C. Koningsberger and R. Prins, eds. (John Wiley, New York, 1988), pp. 119-161.

14. W. H. McMaster, N. Kerr del Grande, J. H. Mallett, and J. H. Hubbell, *Compilation of X-ray Cross-Sections*, UCRL-50174, Sec. II Rev. 1: Obtain from Clearing House, U.S. Dept of Commerce, Springfield, VA 22151.

15. G. Bunker, "Sources of Noise in EXAFS Experiments," from the series *Basic Techniques for EXAFS*, (National Biostructures PRT, unpublished, 1988).

16. J. J. Rehr, J. Mustre de Leon, and S. I. Zabinsky, J. Amer. Chem. Soc., **113**, 5135 (1991).

17. J. Mustre de Leon, J. J. Rehr, and S. I. Zabinsky, Phys. Rev. B, **44**, 4146 (1991).

18. J. J. Rehr, R. C. Albers, and J. Mustre de Leon, Physica B, **158**, 417 (1989).

19. *Structure Reports*, **16**, 541, (1952); **26**, 760, (1961).

20. D. E. Sayers, F. W. Lytle and E. A. Stern, J. Non-Cryst. Solids, 8-10, 409 (1972).

21. R. Pachter, H. Jiang, unpublished. In preparation for *Computational Polymer Science*.

22. D. E. Sayers, S. M. Heald, M. A. Pick, J. I. Budnick, E. A. Stern, and J. Wong, Nucl. Inst. Meth., 208, 631 (1983).

23. S. M. Heald, M. A. Pick, J. M. Tranquada, D. E. Sayers, J. I. Budnick, E. A. Stern, J. Wong, G. Stuckey, A. Chester, G. Woolery, and T. Morrison, Nucl. Inst. Meth., A246, 120 (1986).

24. S. M. Heald and D. E. Sayers, Rev. Sci. Instrum., 60, 1932 (1989).

25. J. D. Jackson, *Classical Electrodynamics*, (Wiley, New York, 1975), pp. 654-683.

26. D. Mills and V. Pollock, Rev. Sci. Instrum., 51, 1664 (1980).

27. J. A. Golovchencko, R. A. Levesque, and P. L. Cowan, Rev. Sci. Instrum., 52, 509 (1981).

28. A. Krolzig, G. Materlik, M. Swars, and J. Zegenhagen, Nucl. Inst. Meth., 219, 430 (1984).

29. C. Y. Yang, J. E. Penner-Hahn, and P. M. Stefan, Nucl. Inst. Meth., A291, 157 (1990).

30. J. J. Rusek, K. P. Chaffee, D. Cooke, Propulsion Directorate, OLAC Phillips Laboratory, Edwards AFB, CA 93523-5000.

31. International Tables for X-ray Crystallography, K. Lonsdale, ed. (Kynoch Press, Birmingham, UK, 1972), Vol 3, p. 161.

32. D. E. Sayers and B. A. Bunker in *X-ray Absorption: Principles, Applications, Techniques of EXAFS, SEXAFS, and XANES*, D.C. Koningsberger and R. Prins, eds. (John Wiley, New York, 1988), pp. 211-253.

33. J. W. Cook, Jr. and D. E. Sayers, J. Appl. Phys., 52, 5024 (1981).

34. T. S. Ertel, H. Bertagnolli, S. Hückmann, U. Kolb, and D. Peter, Appl. Spectroscopy, 46, 690 (1992).

35. B. -K. Teo and P. A. Lee, J. Am. Chem. Soc., 101, 2815 (1979).

36. A. G. McKale, B. W. Veal, A. P. Paulikas, S. -K. Chan, and G. S. Knapp, J. Amer. Chem. Soc., 110, 3763 (1988).

37. P. R. Bevington, Data Reduction and Error Analysis for the Physical Sciences (McGraw-Hill, New York, 1969), p. 204.